New insights into solidification and phase equilibria in the Al-Al_3Zr system: theoretical and experimental investigations

A.V. Khvan[a)], D.G. Eskin[b, c)], K.F. Starodub[a)], A.T. Dinsdale[b)], F. Wang[b)], C. Fang[b)], V.V. Cheverikin[a)], M.V. Gorshenkov[a)]

[a] Thermochemistry of Materials SRC, NUST MISIS, 4 Leninskiy Prosp., Moscow 119049, Russia

[b] BCAST, Brunel University London, Uxbridge UB8 3PH, United Kingdom

[c] Tomsk State University, 36 Lenin Avenue, Tomsk 634050, Russia

Abstract

Phase equilibria and phase transformations during the solidification of alloys in the Al-Al_3Zr corner of the Al-Zr system were investigated using both theoretical (DFT and Calphad modelling) and experimental techniques. This work involved two separate teams investigating the phase transformations of alloys of different compositions during solidification at slow cooling rates using DTA, SEM, TEM, XRD, EPMA analysis of as-cast and annealed samples.

The formation of eutectic type colonies at the boundaries of dendrites and three types of primary intermetallic phase crystals were detected in the examined samples. A eutectic reaction was implied from the results of a DTA analysis. The obtained results question the currently accepted phase diagram for this part of the system which was based on measurements of the solubility of Zr in the aluminium solid solution and the liquidus surface.

Keywords: Al_3Zr, eutectic reaction, Al solid solution, DTA, microstructure analysis

1. Introduction

The Al-Al_3Zr region of the Al-Zr phase diagram has been of particular interest for many

decades due to the industrially important strengthening and anti-recrystallizing effects of additions of Zr to aluminium alloys [1-4].

These effects are achieved by the complete suppression of the formation of primary Al_3Zr-$D0_{23}$ crystals in these alloys at relatively high but still typical casting cooling rates, leading to the formation of a supersaturated solid solution, followed by the formation of coherent or semi-coherent Al_3Zr-$L1_2$ precipitates during annealing.

At the same time much work was carried out to analyse the grain refinement of aluminium alloys resulting from the formation of fine compact particles of the primary Al_3Zr phase [2-3, 5]. Two types of the crystals were observed. Coarse large crystals forming at slow cooling rates were identified as Al_3Zr-$D0_{23}$, while more compact "flower" type crystals were reported as either the metastable Al_3Zr-$L1_2$ phase or a "new phase" [2, 5]. However, there has been no detailed analysis of the formation of these primary crystals and their subsequent transformation.

Finally, the most recent investigation showed the presence of eutectic-type colonies forming at slow cooling at dendrite boundaries [6], and this seems to contradict the previously accepted view that the invariant reaction between the aluminium solid solution, the liquid phase and Al_3Zr-$D0_{23}$ is peritectic in nature. However, the details associated with this observed eutectic behaviour and the compositions of the phases in equilibrium were not previously determined.

2. Critical evaluation of literature data on the invariant equilibria between Al, Al_3Zr and liquid phases.

The phase diagram and thermodynamic properties of the Al-Zr system have recently been critically assessed by Fischer and Colinet [7] (Fig. 1). In the Al-rich side of the phase diagram the assessment reinforces the accepted view that there is a peritectic

reaction between Al_3Zr and the fcc Al-based solid solution. This view is essentially based on the experimental data for the liquidus and solvus [8-14]. According to the published experimental data the solubility of Zr in the liquid phase at the melting point of Al is lower than that in the Al-based solid solution. There are a number of sets of experimental data for the liquidus in concentrated aluminium alloys, the most recent [8] being reported after the work of Janghorban et al. [9], but these are also consistent with the earlier work of Chiotti and Woerner [10] and Fink and Willey [11] and with the calculated phase diagram [7]. Extrapolating these experimental results down to the invariant temperature (whether it is a eutectic or a peritectic reaction) gives a mole fraction of Zr in the liquid of 0.0003 (Fig. 1). There is rather more scatter in the experimental data for the solvus [11-14] which are derived from microstructural examination, and studies of hardness and electrical resistivity on quenched samples. It is felt that these are likely to be unreliable because of the known ability of Zr to supersaturate in aluminium [15]. Hence, the quenching, especially from the liquid state, may not be the right technique to assess the equilibrium solubility. Also the annealing times to reach equilibrium in this system are rather long (as we show below in this paper) and have not been used in the previously reported research. However, based on these data, Fischer and Colinet [7] estimated the solubility of Zr in the fcc Al solid solution to be approximately 0.0008 in terms of the mole fraction of Zr. Clearly if the composition of Zr in the solid solution is higher than that in the liquid phase the reaction must be peritectic in nature.

However, this view of the phase diagram is not consistent with the recent paper of Janghorban et al. [9] who observed thermal arrests for a sample containing 1 at.% (3.3 wt%) Zr at 927 and 929 K (654 and 656 °C). This was obtained via careful thermal

analysis involving pure Al reference samples. These results indicated a eutectic reaction with the invariant temperature approximately 5 K below the melting point of Al. These authors also referenced the paper by McPherson and Hansen [16] which reported a study of the Al-Zr system by thermal analysis. A thermal arrest had been reported for a sample containing 6.4 at.% (18.7 wt%) Zr at 928 K (655 °C) although there had been no discussion of this particular measurement. Janghorban et al. [9] ascribed the discrepancy between the observed eutectic behaviour and the peritectic deduced from solubility measurements as due to errors in the measurement of the liquid compositions, i.e. the Zr content of the liquid in equilibrium with Al_3Zr.

In order to clarify the phase equilibria and the nature of the phase transformation, we have performed additional experiments which are reported in this current paper. These experiments are supported by ab-initio and thermodynamic calculations.

3. Methodology

3.1 DFT and Calphad calculations

Ab initio

In order to provide extra insight into the solubility of Zr in the fcc Al solid solution, calculations were carried out using *ab-initio* density functional theory in supercells to estimate the partial enthalpy of solution of Zr in fcc Al to compare with the critically assessed parameters of Fischer and Colinet [7]. These were undertaken using the plane wave method implemented in the Vienna *Ab initio* Simulations Package (VASP v. 5.3.5) [17-18]. The Projector-Augmented Wave (PAW) framework was employed [19] within the Generalised Gradient Approximation (GGA) [20, 21]. Experience has shown that GGA is well suited to describe the properties of transition metals [22, 23]. High cut-off energies for the wave functions (550.0 eV) and the augmentation functions

(700.0 eV) were employed in order to obtain reliable total-valence electron energies. The electronic wave functions were sampled on dense grids, in the irreducible Brillouin zone (BZ) for the crystals, using the Monkhorst and Pack method [24]. We performed calculations for one Zr atom in a basic Al fcc lattice of size $2a_0 \times 2a_0 \times 2a_0$ ($Al_{31}Zr$), $3a_0 \times 3a_0 \times 3a_0$ ($Al_{107}Zr$) and $4a_0 \times 4a_0 \times 4a_0$ ($Al_{255}Zr$) where a_0 is the lattice parameter of a conventional fcc Al lattice. To get accurate formation energies for the dilute solution of Zr in Al, we used the same cells and k-mesh for pure Al as reference to minimize any systematic errors.

Calphad calculations

For the Calphad calculations the MTDATA software package was used. The assessment of Fischer and Colinet [7] was used as a starting point. The *ab-initio* DFT calculations results were used to compare the assessed enthalpy of mixing in the fcc phase with what might be justified theoretically. It should be pointed out that the excess of entropy of Fischer and Colinet [7] was used unchanged.

3.2 Experimental

The experimental work at MISIS was concerned with differential thermal analysis (DTA) and studying primary crystals by scanning electron microscopy (SEM), electron back scattered diffraction (EBSD), transmission electron microscopy (TEM) and electron probe microanalysis (EPMA). Experimental effort at Brunel University London (BCAST) was concerned with studies on crystals at grain boundaries using SEM and TEM.

Preparation of samples

The purity of the starting materials for samples prepared at MISIS was 99.99 wt% Al

and 99.99 wt% Zr. Alloys with 0.04 and 0.30 at.% (0.15 and 1 wt%) Zr were prepared in an electric resistance furnace Nabertherm LF 30/14 in graphite crucibles. The melt was held at 1273 K (1000 ºC) for 2 hours, mixed by crucible rotation (without introducing any stirring rods in order to avoid contamination or overcooling of the melt) and then left to solidify in a crucible covered with heated refractory bricks to reduce heat losses in air (for alloys with 0.30 at.% (1 wt%) Zr). The cooling rate in the central part of the sample was ~5 K/min in the temperature range 973-773 K (700-500 °C). The resulting samples had a mass of about 170 g and were cut in half. Samples from the mid-section were taken for microstructural and differential thermal analysis (Fig. 2). The final compositions of the specimens used for the analysis were additionally determined by EDX prior to the TEM experiments.

For the specimens used at BCAST high-purity 99.95 wt% Al (~750 g for each experiment) was melted in a clay-bonded graphite crucible inside an electrical resistance furnace and heated up to 1173 ± 3 K (900 ± 3 ^{o}C), at which point an Al-10 wt% Zr master alloy was added with mechanical stirring to obtain a range of alloys with 0.03 to 0.15 at.% (0.1 to 0.5 wt%) Zr alloy. The melt was then isothermally held for 1 hour with intermittent stirring before it was taken out of the furnace to solidify in a crucible to room temperature with a cooling rate around 1 K/s as measured by K-thermocouples.

For the Al-0.12 at.% (0.4 wt%) Zr alloy, additional experiments were carried out by casting the melt into a wedge mould placed in an electrical resistance furnace which was used to preheat the wedge mould to 773 K (500 ^{o}C) and then switched off during the casting and solidification. The casting temperature was around 1123 K (850 ^{o}C) and the cooling rate range obtained with this particular setup of wedge mould in a switched-off

furnace was from 3 to 12 K/s as estimated from the cooling curves recorded by K-type thermocouples placed along the axis of the mould.

The ingots solidified in the crucibles were longitudinally sectioned along the central symmetrical axis and specimens were prepared from the central bottom part because it was felt that most of the primary Al_3Zr particles would settle down to the bottom of the ingot during solidification due to the larger density of Al_3Zr and the slow cooling rate. For the wedge-mould ingots, specimens were cut from the bottom along the longitudinal axis to obtain specimens associated with different cooling rates. All the specimens were then mechanically ground and polished for SEM (ZEISS SUPRA 35VP) examination.

Microstructure analysis

Metallographic specimens for microscopic examination were prepared by a grinding-and-polishing machine (Struers Labopol-5). The grinding procedure was carried out with SiC-paper and specialized Struers polishing disks (MD-Mol and MD-Nap) with OP-U colloidal silica suspension. A suspension was applied at regular time intervals during the preparation. The microstructure of the alloy was examined by means of optical microscopy (OM) (Olympus-GX71F-5) and SEM (TESCAN VEGA LMH) with a LaB_6 cathode and an energy dispersive X-ray microanalysis system (Oxford Instruments Advanced AZtecEnergy). A four-crystal wave spectrometer was used during the electron probe microanalysis (EPMA) of all the phases (the analysed particle size was larger than 2 μm). 20 kV was set for the EPMA acceleration voltage.

Transmission electron microscopy (TEM) was carried out using JEM2100 with a LaB_6 cathode operated at 200 kV. Thin electron transparent foils were prepared in two ways depending on the objective. For the observation of fine precipitates in the Al solid solution the foils were prepared by dual-jet electrolytic polishing in a HNO_3-methanol

electrolyte at 253 K (-20 °C). In case there were coarse individual particles, the samples were prepared by a focused ion beam technique (FIB, FEI Quanta-3D) using precision Pt sputtering, Ga^+ ion milling and lift-out procedures.

The FIB technique was also used to prepare TEM thin foils for studying fine particles along grain boundaries. These particles both with and without the presence of large Al_3Zr particles nearby were cut and lifted up using a tungsten manipulator and transferred to an Omni lift-out copper grid in an FEI Quanta 3D FEG dual beam microscope. After the transfer, the relatively thick foils on the copper grid were further thinned by the ion beam step by step to around 80 nm. In total, four foil samples were prepared and examined in a JEOL 2100F TEM operated at 200 kV. Energy-dispersive X-ray spectroscopy was also carried out in the TEM to determine the composition of the tiny particles.

Differential thermal analysis

Phase transition temperatures were measured with a DSC LABSYS from Setaram. The alumina crucibles were used for the experiments. No side reaction between the sample and the crucible was observed. Prior to the experiment, calibration of the apparatus was performed with pure metal standards – 99.999 wt% Pb, 99.99 wt% Al, 99.99 wt% Cu and 99.99 wt% Ag. The error range of the calibration results was ±0.3 K. Due to the fact that the melting temperatures of the analysed Al-Zr samples are very close to the melting point of pure Al, higher weight was put on the calibration values for pure (Al) and all results were analysed in comparison with the melting point of pure Al. The DTA experiments were carried out on as-cast and annealed samples taken from the centre of the ingot in closed Al_2O_3 crucibles under a continuous flow of Ar (99.995% purity, additionally filtered with an oxygen trap). Prior the experiment, the apparatus was

pumped out to 10^{-5} atm. and filled with Ar three times. The heating/cooling rates for calibration and the experiments were 5, 1 and 0.5 K/min. The change in the weight of the samples was less than 0.5% of their initial mass (0.2-0.5mg from 100mg original samples). No reactions between sample and crucible were observed. The samples retained their original metallic sheen.

Experiments were carried out with an empty crucible and with Al as a reference sample. Additional experiments were carried with the sample and reference positions exchanged in order to detect possible differences between the output signals from the thermoelements on different sides of the detector. The DTA heating curves were used to determine the solidus temperatures of the samples at different heating speeds. It should be mentioned here that the DTA cooling curves in this particular case cannot provide accurate results because the Al_3Zr intermetallic particles are heavy and, during slow solidification, fall to the bottom of the crucible (Fig. 3) creating large differences in the concentration thereby reducing equilibrium within the sample.

4. Results of the DFT and Calphad calculations

The calculated *ab-initio* results are listed in Table 1 and compared with the values derived from the available experimental data, which includes, in addition, the calculated lattice parameters and formation enthalpies for 0 K (-273.15 °C) of the various potential phase structures of Al_3Zr. Clearly the calculations reproduce well (within 1 rel.%) the experimental lattice parameters for the elemental solids extrapolated down to 0 K (-273.15 °C) [25] and the Al_3Zr phases [2,5,26-27]. This justifies the present approach and settings.

The present calculations also showed that for Al_3Zr, the $D0_{23}$ phase is the ground state

with a substantially lower energy of formation than the two other phases ($L1_2$ and $D0_{22}$), which agrees with the previous theoretical study [28]. The calculations also showed that the formation energies for the metastable $L1_2$ and $D0_{22}$ phases are very close. This is consistent with the present observations (see the later section on primary phases in Al-Zr alloys) that the Al_3Zr-$L1_2$ and the Al_3Zr-$D0_{22}$ phases may appear at high temperature, as well as upon annealing of quenched samples [2, 5]. It can also be seen from Table 1 that the calculated enthalpy of formation of the $D0_{23}$ structure of Al_3Zr for 0 K (-273.15 °C) is in very good agreement with the assessed data of Fischer and Colinet [7] for 298.15 K (25 °C). It should be noted here that enthalpies of formation generally do not vary significantly with change in temperatures.

As shown in Table 1, the formation energy increases with a reduction in the Zr concentration. Moreover, it should also be noted that the number of configurations (*w*) of the Zr impurity in the cell increases with its size (Table 1). Normalisation of these calculated results can give an estimate of the partial enthalpy of solution of Zr in fcc Al which can then be compared with those from the assessed data of Fischer and Colinet [7]. The *ab initio* values are clearly less negative than the assessed values, which implies that the partial enthalpy of solution varies more markedly with composition. It is not clear at the moment whether this variation of the enthalpy of solution is significant or whether it represents a limitation on the results of the *ab initio* calculations.

A less negative value for the partial enthalpy of solution of Zr in Al suggests a lower solubility of Zr in the solid solution phase. Fisher and Colinet [7] used the parameter G(FCC_A1,AL,ZR:VA;0)=-140764.18+24.15621*T while the value derived in the present work is 13000 more positive, so the new parameter is G(FCC_A1,AL,ZR:VA;0)

=-127764.18+24.15621*T. The effect of changing the parameters for the fcc phase in Fischer and Colinet's assessment in this way is shown in Fig. 4 (although it should be pointed out that the excess entropy of [7] was used unchanged). What is apparent from these thermodynamic calculations is that there is a clear limit on how much the eutectic temperature can be below the melting point of Al. The revised data, shown in Fig. 4, indicates that a reduction of 0.1 K is reasonable. However even if there were no solubility of Zr in fcc Al the maximum reduction that could be obtained would be 0.2 K assuming that the liquidus curve remains unchanged. This is far less than had been obtained in our previous experimental work [6], which is, in turn, less than that found by Janghorban et al. [9]. These results forced us to make a more detailed experimental analysis of the reactions and phase formation in the Al-Al_3Zr region.

5. Experimental results

Fine particles along the grain boundaries

Fig. 5 shows typical SEM backscatter electron (BSE) images of specimens cut from a number of Al-Zr alloy samples with different compositions following solidification in crucibles. As we can see, in addition to typical large primary Al_3Zr particles, there are fine particles clearly visible along the grain boundaries in the alloy samples with 0.09, 0.12 and 0.15 at.% (0.3, 0.4 and 0.5 wt%) Zr. However, no distinct particles could be detected in the alloy samples with 0.03 and 0.04 at.% (0.1 and 0.15 wt%) Zr. It should be noted that the amount of these tiny particles along the grain boundaries increases as the concentration of Zr increases.

Fig. 6 shows typical SEM backscatter electron (BSE) images of specimens solidified at different cooling rates cut from samples of the Al-0.12 at.% (0.4 wt%) Zr alloy cast in the wedge mould. The fine particles along the grain boundaries can only be observed in

specimens solidified with a cooling rate below 5 K/s; no sign of such particles could be observed in the specimen solidified at a cooling rate of 12 K/s. It is also important to point out that no large primary Al_3Zr particles could be detected in samples of the Al-0.12 at.% (0.4 wt%) Zr alloy cast in the wedge mould even with the slowest cooling rate as shown in Fig. 6(a).

The identity of the particles observed along the grain boundaries is of great importance for understanding the solidification behaviour of Al-Zr alloys under the current casting conditions. In order to ascertain the identity of these fine particles, foil samples prepared by FIB were examined by TEM. First of all, EDS mapping was done on all the fine particles to determine their compositions. A typical EDS map is shown in Fig. 7. It is clear that the fine particles contain only Al, Zr and small amounts of Cu without any obvious presence of other elements. This therefore excludes the possibility that these particles represent impurities such as oxides, nitrides or carbides. The presence of small amounts of Cu could be attributed to contamination from Cu re-deposition as a result of the milling of Cu grid holder which is used to support the TEM foil sample. This is a common problem with FIB technique.

Although it is determined that these particles contain only Al and Zr, they could still be in the form of one of the following phases: tetragonal Al_3Zr-$D0_{23}$[29], metastable tetragonal Al_3Zr-$D0_{22}$ [5] , metastable cubic Al_3Zr-$L1_2$ [30], Al_2Zr [31] or even Al_3Zr_2 [32]. Therefore, selected area electron diffraction (SADP) patterns at different tilting angles were obtained for all the fine particles in the four examined foil samples. It was found that they can all be indexed as tetragonal Al_3Zr-$D0_{23}$ phase [5] as illustrated in Fig. 8 which shows a series of SADP patterns obtained from a representative tiny particle at different tilting angles. The tilting angles from Fig. 8(b) and 8(c) and from

Fig. 8(b) to 8(d) are 6.57^{o} and 10.97^{o}, respectively. They agree well with the angles between corresponding beam directions which are 6.38^{o} and 10.69^{o}, respectively. Combining the EDS mapping results with the SADP patterns analysis, it was concluded that the fine particles observed along the grain boundaries are tetragonal Al_3Zr-$D0_{23}$ particles. It is interesting to point out that the tetragonal Al_3Zr-$D0_{23}$ phase is the equilibrium primary phase shown in the binary Al-Zr phase diagram.

The experimental results shown above provide evidence from microstructure determination that a eutectic reaction takes place upon solidification of aluminium rich Al-Zr alloys. This is not consistent with the accepted phase diagram for the system.

Primary phases in Al–Zr alloys

The previous sections show that solidification of Al rich Al-Zr alloys exhibits features normally expected of eutectic reactions. In this section we explore this question in more detail by analysing the microstructures of the "hypereutectic alloy" Al-0.3 at.% (1 wt%) Zr where a large fraction of the primary intermetallic crystals forms. Through this we hope to gain a more detailed understanding of the behaviour and possible transformations in the intermetallic phase. Three different types of intermetallic primary crystals were observed (Fig. 9-12), and this means that the as-cast samples are in a non-equilibrium state and that metastable intermetallic phases may have been formed instead of the stable ones. This made it necessary to analyse the structure of these crystals and the phase transformations which take place during long annealing times while the equilibrium is being reached.

Fig. 9 shows the microstructure of the as-cast sample I, taken from the mid-section of the ingot (Fig. 2). Fig. 9 (a) and (b) are SEM images of the part of the sample close to the crucible bottom or walls, while 9 (c) and (d) are images from the part closest to the

centre of ingot. As can be seen from these images, the higher cooling speed associated with being close to the walls of the crucible and faster nucleation near the crucible walls (in comparison to nucleation within the bulk melt), coupled to the gravitation effect (the particles of Al_3Zr-$D0_{23}$ nucleating in the liquid are heavy) promotes the formation of Al_3Zr phase in the form of significantly larger crystals (Fig. 10a). The electron back-scattered diffraction (EBSD) analysis of these crystals determined them to be Al_3Zr-$D0_{23}$ phase (Fig. 10b). Different colours in Fig. 10b correspond to phases with different crystallographic lattices. The phase marked with the blue colour has reflections of Kikuchi lines corresponding to the aluminium solid solution (fcc_A1), while the green coloured phase had Kikuchi lines corresponding to the Al_3Zr-$D0_{23}$. Closer to the centre of the ingot, where the cooling speed is lower, Al_3Zr crystals with a more compact form start to appear as well, and the degenerate eutectic appears. In the previous paper the cooling rate range where the eutectic appears was determined to be 0.5 to 5 K/s [6].

In addition to the stable Al_3Zr-$D0_{23}$ type of intermetallic primary crystals, two other types of crystals were found: “flower crystals” (Fig. 11a) and “porous Al_3Zr crystals” (Fig. 12a) which frequently form either separately or in the middle of the flower crystal (Fig. 12b).

The amount of Zr in the “petals” of the “flower crystals” is, according to EPMA, about 6.5 - 9.0 at.% (19.0–25.1 wt%) close to the centre, and about 3.0 - 6.0 at.% (9.5–17.8 wt%) on the edges, which does not correspond to any known phase in the system. The results of the TEM investigations of the porous crystals in the central part of the “flower crystals” are shown in Fig. 11. A selected area electron diffraction pattern (SADP) associated with the central portion is shown on Fig. 11b. The SADP reveals that this central part consists predominantly of the stable Al_3Zr-$D0_{23}$ phase, fcc_A1 (Al), and

traces of the Al_3Zr-$L1_2$ phase. The diffraction pattern in Fig. 11b represents the orientation relation where the [001]-axis *c* of tetragonal Al_3Zr-$D0_{23}$ is parallel to the [001] fcc A1 (Al) and [001] Al_3Zr-$L1_2$ axes respectively. The right part of Fig. 11b shows a simulated image of a diffraction pattern with the abovementioned orientation relationship. The kinematically forbidden reflections (002, 006 …) of the tetragonal phase are not marked despite their existence on the obtained diffraction pattern due to dynamical character of electron scattering. The bright-field and dark-field images of the Al_3Zr-$D0_{23}$ phase in Figure 11c and 11d show that the central part of the analyzed crystal is not monocrystalline but consists of colonies of the Al_3Zr-$D0_{23}$ phase with different orientations but with almost the same orientation within a colony.

Investigations of the bright-field images and diffraction pattern of the "petals" of the "flower crystal" showed that they consist of (Al) fcc A1, Al_3Zr-$L1_2$ and traces of the Al_3Zr-$D0_{23}$ phase (Fig. 11d-f). The [001] direction – *c*-axis of Al_3Zr-$D0_{23}$ is parallel to [100] (Al) fcc_A1 and [100] Al_3Zr-$L1_2$ axes. The presence and intensity of the superstructure reflections corresponding to the Al_3Zr-$L1_2$ phase indicate the predominance of this phase in the structure of the "petals". The Al_3Zr-$L1_2$ precipitates are elongated along [01-1]. This was also confirmed by observations in the dark-field of reflections corresponding only to the Al_3Zr-$L1_2$ phase (010) and in reflections corresponding to the superposition of the (011) Al_3Zr-$L1_2$ and Al_3Zr-$D0_{23}$ phases. The amount of the Al_3Zr-$D0_{23}$ phase in the petals appears to be negligible.

It should be noted that the structure of the petals showed that they are also not monocrystalline, but form colonies (Fig. 11e).

In order to understand which of the intermetallic phases is stable the samples were annealed at 927 K (654 °C) for 144 h. Subsequent analysis showed complete

transformation of the Al_3Zr-$L1_2$ crystals into Al_3Zr-$D0_{23}$ both in the centre and in the "petals", and this was confirmed by TEM structure investigations shown in Fig. 13. Fig. 13a represents a secondary electron image of the "flower crystal" obtained by FIB. The place from where the sample was cut for the TEM investigations is marked by a dashed line. The bright-field TEM micrograph and enlarged HRTEM images of the thin lamella precisely milled by FIB are shown on Fig. 13 b and 13 c. The elongated precipitates along the [010] and [001] Al directions are seen on a bright-field image. The circles with numbers 1, 2 and 3 depict the places corresponding to the SADPs in Fig. 13 d-f, respectively. The diffraction patterns in Fig. 13 d-f are associated with an fcc Al crystal along the [100] zone axis, and two variants of Al_3Zr-$D0_{23}$ orientations in Al corresponding to the *c*-axis ∥ [001] Al and *c*-axis ∥ [010] Al. It is seen that elongation of the Al_3Zr-$D0_{23}$ precipitates occurs along the *c*-axis and parallel to {001} Al directions. According to the TEM investigations, both the central part and the "petals" are the equilibrium Al_3Zr-$D0_{23}$ phases and consequently the complete decomposition of the metastable crystals indicates that the equilibrium state of the alloy has been reached.

The SEM images of the "porous crystals" are shown in Fig. 12a and 12b. The bright-field image from a central portion cut by FIB and the associated diffraction pattern indexed as the Al_3Zr-$D0_{23}$ [010] zone axis are shown in Fig. 12c. The «pores» are not true voids: they are filled with aluminium.

These observations of metastable intermetallic phases and their transformation during annealing could be explained by the formation of clusters within the liquid of aluminium atoms supersaturated with Zr or the metastable Al_3Zr-$L1_2$ phase during solidification possibly due to an incomplete diffusion processes taking place in the liquid phase. These crystals undergo a cellular type decomposition during cooling. The

presence of the Al_3Zr-$D0_{23}$ phase in the traces of the petals indicates that transformation should finally lead to the formation of the stable Al_3Zr-$D0_{23}$ phase. A possible reaction path is: supersaturated fcc A1 (Al)/ Al_3Zr-$L1_2$→ Al_3Zr-$L1_2$+ fcc A1 (Al)→ Al_3Zr-$D0_{23}$ +fcc A1 (Al).

Finally, for the better understanding of the phase relations in this corner of the phase diagram of the Al-Zr system it was necessary to understand whether the previously reported solubility of Zr in the aluminium solid solution is correct or too high (see the section Results of DFT and Calphad calculations). In order to analyse the solubility of Zr in the Al solid solution, a sample with 0.04 at.% (0.15 wt%) Zr was prepared, which is below the maximum solubility of Zr in fcc Al proposed in [7, 28]. The sample was annealed at 927 K (654 °C) for 42 h and quenched in water. A TEM analysis showed the formation of the Al_3Zr-$L1_2$ precipitates (Fig. 14) with the «zero contrast line» parallel to the [001] Al direction. The presence of such precipitates indicates that a shift of the solvus line towards lower concentration of Zr than suggested by Fischer and Colinet [7] is necessary. The version of the eutectic phase diagram in Fig. 4 makes the formation of these Al_3Zr particles quite logical. The fact that the phase is metastable at this temperature indicates that the precipitation of Al_3Zr at such low contents of Zr is slow and the alloy does not reach equilibrium. According to the classical theory of nucleation [33], the growth rate of particles is in direct ratio to solute saturation. The formation of very fine metastable Al_3Zr-$L1_2$ particles can be the reason why the precipitation has not been identified by SEM analysis in previous investigations as these particles could not be seen at such resolution. Furthermore, their small amount makes them effectively invisible to the electric resistance and hardness methods used previously for the determination of solubility.

Results of the DTA investigations

The experimental DTA results described in section 2 appear to indicate that the invariant reaction close to pure Al is a eutectic rather and a peritectic. However, it is also possible that the decrease in the temperature of the invariant reaction relative to the melting point of Al could be the result of the presence of the metastable phase Al_3Zr-$L1_2$ in the as-cast state. For this reason, a further DTA analysis was carried out on samples that had been annealed for long periods and had shown only Al_3Zr-$D0_{23}$ phase precipitates in addition to (Al). This new investigation confirmed that the invariant reaction is below the melting point of Al indicative of a eutectic reaction. However, this decrease in temperature was smaller than that obtained from measurements on the as-cast material which we believe was due to the formation of metastable phases in the as-cast samples (Table 2, Fig. 15).

In carrying out these measurements it was found that care had to be taken in interpreting results where samples were placed either in the reference pan or in the standard sample position. In our studies on Al-Zr alloys the DTA measurements were carried out firstly with pure Al as a reference material in the standard position of the crucible (the sample on the sample side with pure Al on the reference side), and secondly in the opposite configuration (the sample on the reference side and Al in the sample position). These measurements gave contradictory results. For this reason, we carried out additional experiments where both crucibles were filled with samples of pure aluminium of equal weight and shape in order to detect any possible differences between the signal output from the two sets of thermoelements. It appeared that the signal on the reference side is delayed (see Fig. 15c). This means that, in practice, the contradictory results mentioned above were because of the detector delay rather than due to the melting of the

aluminium at a lower temperature than that of the sample. It also means that this technique should be used only with a great deal of care. Further measurements were carried out with the sample on the sample side and an empty crucible on the reference side and in the opposite configuration in order to confirm the invariant temperature (see Table 2).

In conclusion, the results of DTA measurements on annealed samples are consistent with the microstructural results on the fine particles found at the grain boundaries, and on the primary phases themselves. They confirm that the invariant reaction close to pure Al in the Al-Zr system is indeed eutectic in nature in contrast to the peritectic reaction shown in the currently accepted binary phase diagram.

Conclusions

- *Ab initio* calculations carried out in the present work indicate that that the enthalpies of solution of Zr in fcc_Al (Al) are less negative than the critically assessed values of Fischer and Collinet [7].
- A less negative value for the partial enthalpy of solution of Zr in Al implies a lower solubility of Zr in the fcc solid solution phase. The effect of changing the parameters for the fcc phase in Fischer and Colinet's assessment to reflect the *ab initio* results is demonstrated although the excess entropy was not changed. It is apparent from these calculations that there is a limit on how much the eutectic temperature can be below the melting point of Al. The revised data indicates that a reduction of 0.1 K is reasonable. However, even if there was no solubility of Zr in fcc A1 (Al) the maximum reduction that could be obtained would be 0.2 K assuming that the liquidus curve remains unchanged.
- A DTA analysis of as-cast samples identified a temperature arrest at 932.2 K

(659 °C). More refined DTA analyses on samples annealed for long times showed the thermal arrest to be close to 933.1 K (659.9 °C). The discrepancy between these results is thought to be due to lack of equilibration of the as-cast samples and the formation of metastable phases. This correlates well with the thermodynamically predicted decrease of the invariant reaction temperature using the results of *ab initio* calculations. The experimentally determined temperature is lower than the melting point of pure aluminum, which confirms the presence of a eutectic reaction.

- Three types of primary intermetallic crystals were found. They were identified as: (a) stable Al_3Zr-$D0_{23}$, (b) colonies of the metastable mixture Al_3Zr-$D0_{23}$+fcc A1 (Al)+traces of Al_3Zr-$L1_2$ phase ("porous crystals") and (c) colonies of the metastable decomposed mixture Al_3Zr-$L1_2$ phase+fcc A1 (Al)+traces of Al_3Zr-$D0_{23}$ ("flower crystals")
- It is suggested that during solidification, supersaturated crystals of (Al) or the Al_3Zr-$L1_2$ phase form possibly due to incomplete diffusion processes in the liquid phase. These crystals undergo decomposition during cooling.
- A TEM analysis of an Al-0.04 at.% (0.15 wt%) Zr sample annealed at 927 K (654 °C) for 42h and subsequently quenched showed the presence of precipitates of the metastable Al_3Zr-$L1_2$ phase. This suggests for equilibrium conditions the solubility of Zr in the aluminium solid solution should be lower than previously observed. This was also predicted by a thermodynamic analysis of the results of *ab initio* calculations.

Acknowledgements

The Russia-based team acknowledge financial support from the Ministry of Education

and Science of the Russian Federation, Contract No14.581.21.0017, dated on 02nd of November 2015, Unique number RFMEFI58115X0017.

The UK-based authors acknowledge financial support from the Engineering and Physical Sciences Research Council (EPSRC) for the UltraCast project (Grant EP/L019884/1) and the LiME Hub (Grant EP/N007638/1).

References

[1] N. Ryum, Precipitation and recrystallization in an Al-0.5wt%Zr-alloy, Acta Metallurgica 17 (1969) 269–278.

[2] J.Q. Guo, K. Ohtera, K. Kita, T. Shibata New metastable phases in rapidly solidified Al-Zr and Al-Ti alloys with high solute contents. Materials Science and Engineering; A 181-182 (1994) 1397-1404.

[3] T.V. Atamanenko, D.G. Eskin, M. Sluiter, L. Katgerman, On the mechanism of grain refinement in Al-Zr-Ti alloys, Journal of Alloys and Compounds 509 (2011) 57–60.

[4] F.Wang, D. Qiu, Z.-L. Liu, J.A. Taylor, M.A. Easton, M.-X. Zhang, Acta Materialia 61 (2013) 5636–5645

[5] J.Q. Guo, K. Oheta, An intermediate phase appearing in $L1_2$-Al_3Zr to $D0_{23}$-Al_3Zr phase transformation of rapidly solidified Al-Zr alloys. Materials Letters 27 (1996) 343-347.

[6] F. Wang, D.G. Eskin, A.V. Khvan, K.F. Starodub, J.J.H. Lim, M.G. Burke, T. Connolley, J.Mi, On the occurrence of a eutectic-like structure in solidification of Al-Zr alloys. Scripta Materialia 133 (2017) 75–78.

[7] E. Fischer, C. Colinet, An Updated Thermodynamic Modeling of the Al-Zr System.

Journal of Phase Equilibria and Diffusion. 36(5), 2015, 404-413

[8] O. Dezellus, B. Gardiola, J Andrieux, On the Solubility of Group IV Elements (Ti,Zr,Hf) in Liquid Aluminum below 800°C, Journal of Phase Equilibria and Diffusion, 35(2) (2014)120-126

[9] A. Janghorban, A. Antoni-Zdziobek, M. Lomello-Tafin, C. Antion, Th Mazingue, A. Pisch, Phase Equilibria in the Aluminium-Rich Side of the Al-Zr System, Journal of Thermal Analysis and Calorimetry, 114(3) (2013) 1015-1020

[10] P. Chiotti, P.F. Woerner, Metal Hydride Reactions: I. Reaction of Hydrogen with Solutes in Liquid Metal Solvents, Journal of the Less Common Metals. 7 (1964) 111-119.

[11] W. L. Fink, L. A. Willey, Equilibrium relation in Al-Zr alloys, Transactions of the Metallurgical Society of AIME, 1 (1939) 69-80

[12] M. E. Drits, E. S. Kadaner, V. I. Kuzmina, Solubility of Silicon and Zirconium in Aluminium, Izvestia Akademii nauk SSSR. Metally, 1 (1968)170-175.

[13] G.M. Kuznetsov, A.D. Barsukov, M.I. Abas, Solubility of Mn, Cr, Ti, and Zr in Al in the Solid State, Soviet Non-Ferrous Metals Research, 11 (1983) 11 47-51.

[14] V. M. Glazov, G. Lazarev, N. Korolkov, The solubility of certain transition metals in aluminium, Metal Science and Heat Treatment, 10 (1959) 48-50.

[15] Z. A. Chaudhury, C. Suryanarayana, A TEM study of decomposition behaviour of a melt-quenched Al–Zr alloy, Metallography 17 (1994) 231–52

[16] D. J. McPherson, M. Hansen, The system Zr–Al, Transactions ASM. 46(1954) 354–74.

[17] G. Kresse, J. Hafner, Ab initio molecular-dynamics simulation of the liquid-metal–amorphous-semiconductor transition in germanium, Physical Review B, 49(1994)

14251- 14269.

[18] G. Kresse, J. Furthmller, Efficiency of ab-initio total energy calculations for metals and semiconductors using a plane-wave basis set, Computational Materials Science 6(1996) 15-50.

[19] P.E. Blöchl, Projector augmented-wave method, Physical Review B, 50(1994) 17953-17979

[20] G. Kresse, D. Joubert, From ultrasoft pseudopotentials to the projector augmented wave method, Physical Review B, 59 (1999) 1758-1775.

[21] J.P. Perdew, K. Burke, M. Ernzerhof, Generalized Gradient Approximation Made Simple, Physical Review Letters, 77(1996) 3865-3868.

[22] C.M. Fang, M.A. van Huis, M.F.H. Sluiter, H. Zandbergen, Stability, structure and electronic properties of γ-$Fe_{23}C_6$ from first-principles theory, Acta Materialia, 58 (2010), 2968-2977.

[23] C. Amador, R.L.W.L. Lambrecht, B. Segall, Application of generalized gradient-corrected density functionals to iron, Physical Review B, 46 (1992) 1870-1873.

[24] H.J. Monkhorst, J.D. Pack, Special points for Brillouin-zone integrations, Physical Review B, 13 (1976) 5188-5192.

[25] J. Arblaster, Private communication, 2017

[26] Y. Ma, C. Roeming, B. Lebech, J. Gjeonnes, J. Taftoe, Structure refinement of Al_3Zr using single-crystal X-ray diffraction, powder neutron diffraction and CBED, Acta Crystallographica B, 48 (1992) 11-16.

[27] G. Brauer, Ueber die Kristallstruktur von $TiAl_3$, $NbAl_3$, $TaAl_3$ und $ZrAl_3$, Zeitschrift für anorganische und allgemeine Chemie. 242 (1939) 1-22.

[28] C. Colinet, A. Pasturel, J. Phase stability and electronic structure in $ZrAl_3$

compound, Journal of Alloys and Compounds 319 (2001) 154-161.

[29] Y. Ma, C. Romming, B. Lebech, J. Gjonnes, J. Tafto. Structure refinement of Al_3Zr using single-crystal X-ray diffraction, powder neutron diffraction and CBED, Acta Crystallographica Section B 48 (1992) 11-16.

[30] E. Nes, H. Billdal. Non-equilibrium solidification of hyperperitetic Al-Zr alloys, Acta Metallurgica, 25 (1977) 1031-1037.

[31] A. Israel, I. Jacob, J.L. Soubeyroux, D. Fruchart, H. Pinto, M. Melamud. Neutron diffraction study of atomic bonding properties in the hydrogen-absorbing $Zr(Al_xFe_{1-x})_2$ system, Journal of Alloys and Compounds. 253–254 (1997) 265-267.

[32] T.J. Renouf, C.A. Beevers. The crystal structure of Zr_2Al_3, Acta Crystallographica, 14 (1961) 469-472.

[33] J.W. Christian. The theory of phase transformation in metals and alloys, Oxford: Pergamon (2002)

Figure captions

Figure 1 - Phase diagram of the Al corner of the Al-Zr system based on the literature review with the phase boundaries calculated using the assessed data of Fischer and Colinet [6].

Figure 2 – Schematic view of the as-cast samples (MISiS).

Figure 3- Alloy Al-0.3 at.% (1 wt%) Zr, sample after the DTA (heat rate 0.5K/min): a) general view b) magnified bottom part (MISiS).

Figure 4 – Comparison of the calculated phase diagram for Al rich corner of the Al-Zr system with the proposed phase diagram based on the present measurements and *ab*

initio results.

Figure 5 - SEM BSE images of the specimens cut from the Al-Zr alloy samples solidified in the crucible with (a) 0.03 at.% (0.1 wt%) Zr; (b) 0.04 at.% (0.15 wt%) Zr; (c) 0.09 at.% (0.3 wt%) Zr, (d) 0.12 at.% (0.4 wt%) Zr and (e) 0.15 at.% (0.5 wt%) Zr (BCAST).

Figure 6 - SEM images of the specimens cut from the Al-0.12 at.% (0.4 wt%) Zr alloy sample cast in the wedge mould at different cooling rates: (a) 3 K/s; (b) 5 K/s; and (c) 12 K/s (BCAST).

Figure 7 - (a) STEM image of a few tiny particles along the grain boundaries; EDS maps of (b) Al; (c) Zr; (d) Cu; (e) O; and (f) Ti (BCAST).

Figure 8 - (a) TEM-BF image of a typical tiny particle at a grain boundary; (b), (c), and (d) SADP patterns obtained from the intermetallic particle and indexed as tetragonal $D0_{23}$ Al_3Zr with beam directions (BDs): (b) $[0\bar{4}\bar{1}]$; (c) $\left[0\bar{5}\bar{1}\right]$ and (d) $[1\bar{5}\bar{1}]$ (BCAST).

Figure 9 - Sample of the alloy Al-0.3 at.% (1 wt%) Zr: a), b) microstructure of the bottom part of the ingot; c), d) microstructure of the central part of the ingot (MISiS).

Figure 10 – Primary Al_3Zr-$D0_{23}$ crystals: a) SEM image in backscattered signal; b) EBSD mapping (MISiS).

Figure 11–TEM micrographs of the structure of the "flower crystals": a) bright-field TEM micrograph of the structure of «flower crystal» at a large scale; b) a [100]Al zone axis diffraction pattern from the central part of the «flower crystal» corresponding to area (c) and a schematic representation of a simulated diffraction pattern where [001] Al_3Zr-$D0_{23}$ is parallel to [001] fcc Al; c) bright-field image of the central part of the «flower crystal»; d) dark-field image of the central part of the crystal taken in (011) Al_3Zr-$D0_{23}$ as image forming reflection; e) Enlarged bright-field micrograph of the

structure of the “petals”; f) a diffraction pattern along [100] Al_3Zr-$L1_2$ zone axis corresponding to the area represented on (e) and a simulated diffraction pattern along [100] fcc Al ∥ [100] Al_3Zr-$L1_2$ and ∥ [001] Al_3Zr-$D0_{23}$ zone axis. The SADP exhibits coexistence of Al_3Zr-$L1_2$, fcc Al and traces of Al_3Zr-$D0_{23}$. (MISiS)

Figure 12 - Structure of the “porous crystals” in the as-cast sample: a) alone; b) inside the “flower crystal” c) a bright-field image of a «porous» crystal from a central part and associated diffraction pattern indexed as Al_3Zr-$D0_{23}$ [010] zone axis (MISiS).

Figure 13 – TEM microstructure of the “flower crystals” in the sample annealed at 927 K (654 °C) for 144h: a) a bright-field image of the thin lamella milled by FIB, the circles with numbers 1, 2 and 3 depict the places corresponding to the SADPs on c), d) and e) images respectively; b) enlarged area with a high-resolution image of $D0_{23}$ crystal; c) a SADP from circle 1 corresponding to Al [100] zone axis; d) a SADP from circle 2 corresponding to Al_3Zr-$D0_{23}$ crystal, c-axis ∥ [001]Al; e) a SADP from circle 3 corresponding to Al_3Zr-$D0_{23}$ crystal, c-axis ∥ [010]Al; f) a secondary electron image of the “flower crystal” obtained in FIB. The place where the sample for investigations was cut is marked by dashed line. (MISiS)

Figure 14 – a) TEM structure of the sample of the alloy Al-0.04 at.% (0.15 wt%) Zr annealed at 927 K (654 °C) for 42 h. The coherent particles with coffee-bean contrast are marked by arrows; b) associated diffraction pattern along [3-10] Al zone axe. The superlattice reflections corresponding to Al_3Zr-$L1_2$ phase are invisible. (MISiS)

Figure 15 – DTA analysis: a) pure aluminium on the reference side; b) pure aluminium on the sample side; c) pure on both the reference and sample sides. (MISiS)

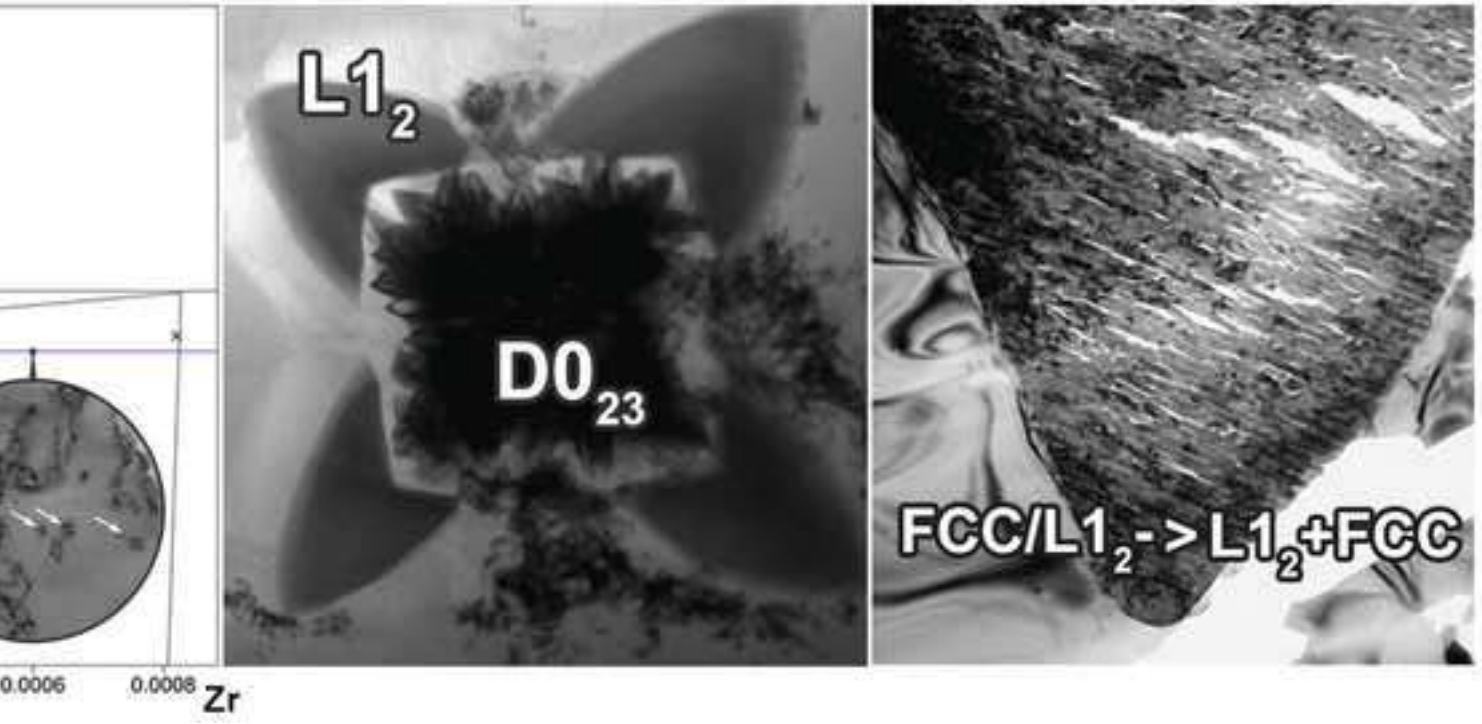
L1$_2$
D0$_{23}$
FCC/L1$_2$ -> L1$_2$+FCC
0.0006
0.0008
Zr

***Highlights (for review)**

- Ab initio calculations carried out for Al-rich part of Al-Zr system.
- The presence of a eutectic reaction confirmed by DTA.
- Three types of primary intermetallic crystals were found.
- Lower solubility of Zr in the aluminium solid solution suggested.

Table 1 - Calculated results from *ab-initio* calculations for the parent elemental solids, the binary Al_3Zr phases and dilute Zr in fcc Al. The experimental values available in the literature are included in parenthesis for comparison. The formation energy (ΔE) is defined as: $\Delta E = E(Al_nZr) - [E(Zr) + nE(Al)]$ with the unit eV per formula (Al_nZr).

Phases	Symmetry /space group (nr)	Lattice parameters (Å)	ΔE (eV/f.u.)	ΔE (eV/kJ mol^{-1})	Assessed [7]
Al	FCC, $Fm\bar{3}m$ (225)	*a*=4.0397 (4.0325 [25])	-		
Zr	HCP, P63/mmc (196)	*A*=3.2316 (3.2288 [25]) *c*=5.1716 (5.1406 [25])	-		
$Al_3Zr\_L1_2$	Cubic,	*a*=4.1047 (4.085 [2]; 4.0656 [5])	-1.850	-178.5	
Al_3Zr-$D0_{22}$	Tetragonal,	*a*=3.9596 (3.8946 [5]) *c*=9.0242 (9.0304 [5])	-1.849	-178.4	
Al_3Zr-$D0_{23}$	Tetragonal, I4/mmm (139)	*a*=4.0167 (3.993 [26]; 4.005 27]) *c*=17.3211 (17.283 [26]; 17.2785 [27])	-1.954	-188.5	-187.12
Compositions of supercell					
$Al_{31}Zr$	Cubic	-	-1.043 (*w*=32)	-100.6	-128.8
$Al_{107}Zr$	Cubic	-	-1.091 (*w*=108)	-105.3	-131.9
$Al_{255}Zr$	Cubic	-	-1.242 (*w*=256)	-119.8	-132.6

Table 2 – DTA results

Alloy	Condition	Heating rate (K/min)	Melting point (°C) [K]	Al melting point, after thermocouple calibration (°C) [K]
Al-1 wt% Zr	As-cast	5	657.2(9) [930.4(4)]	660.33 [933.48]
	As-cast	1	658.4(6) [931.6(1)]	660.32 [933.47]
	Annealed 10 days at 654 °C [927 K]	0.5	659.1(4) [932.2(9)]	660.33 [933.48]
Al-0.15 wt% Zr	Annealed 7 days at 654 °C [927 K]	0.5	660.3(8) [933.5(3)]	660.33 [933.48]
Al-1 wt% Zr	Annealed 6 days at 654 °C [927 K] (measurement carried out on the reference side)	0.5	659.2(6) [932.4(1)]	660.32 [933.47]
Al-1wt%Zr	Annealed 6 days at 654 °C [927 K] (Al-Zr vs Al experiment)	0.1	660.0(5) [933.2(0)]	660.33 [933.48]
	Average from the annealed		659.7 [932.85]	–

mage

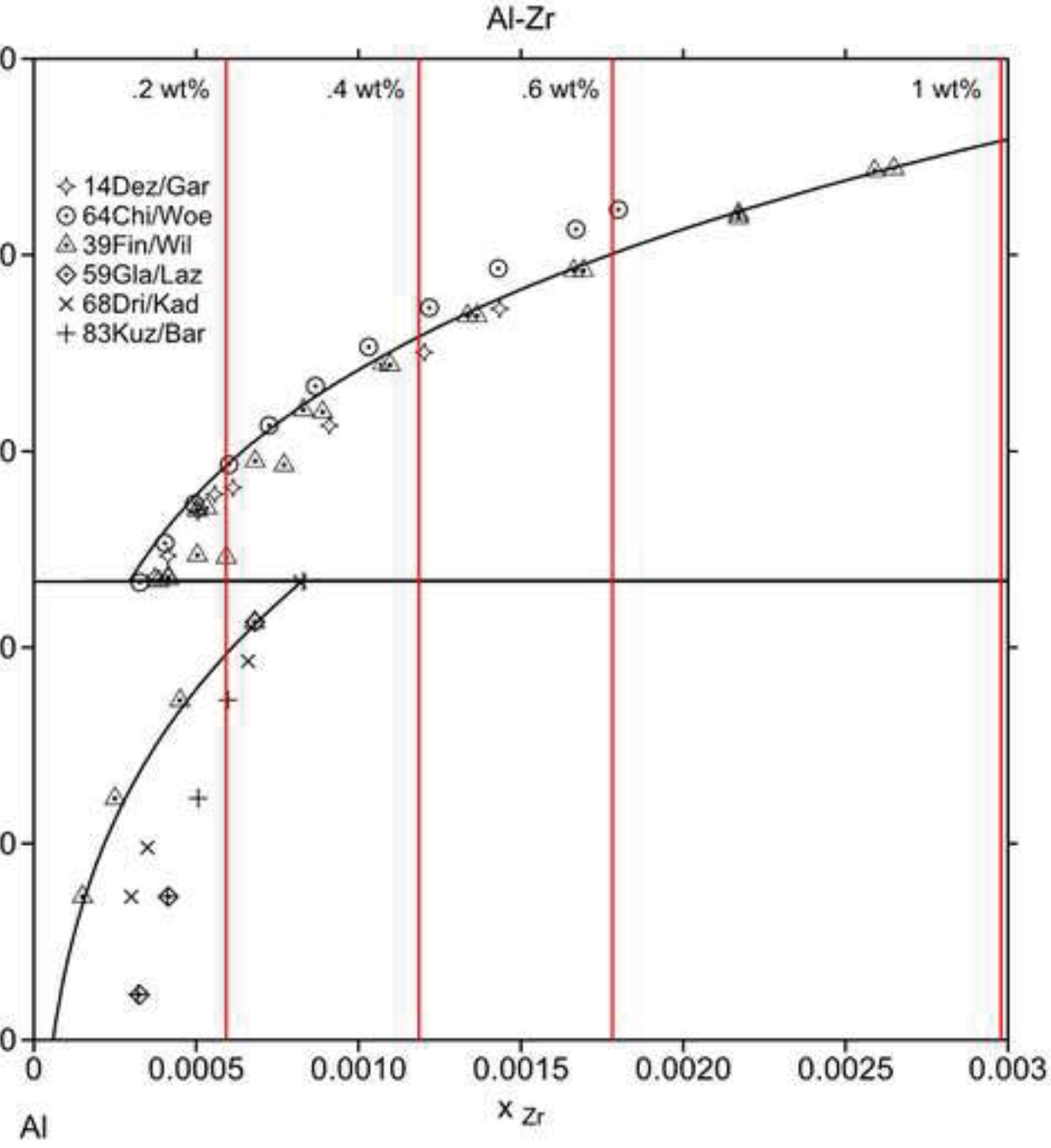
Al-Zr
.2 wt%
.4 wt%
.6 wt%
1 wt%
14Dez/Gar
64Chi/Woe
39Fin/Wil
59Gla/Laz
68Dri/Kad
83Kuz/Bar
0
0.0005
0.0010
0.0015
0.0020
0.0025
0.003
x Zr
Al

mage

ples:

ples

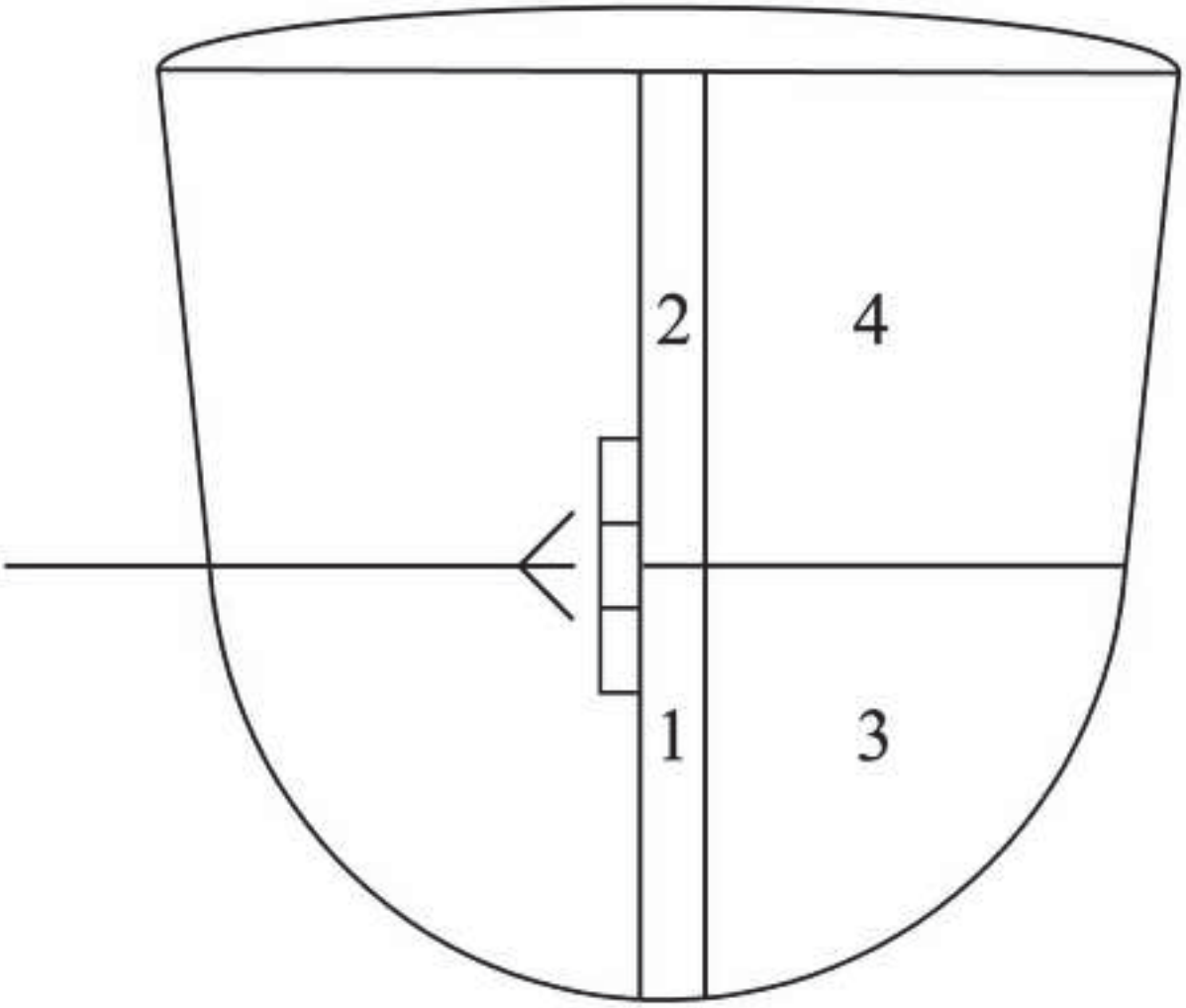

mage

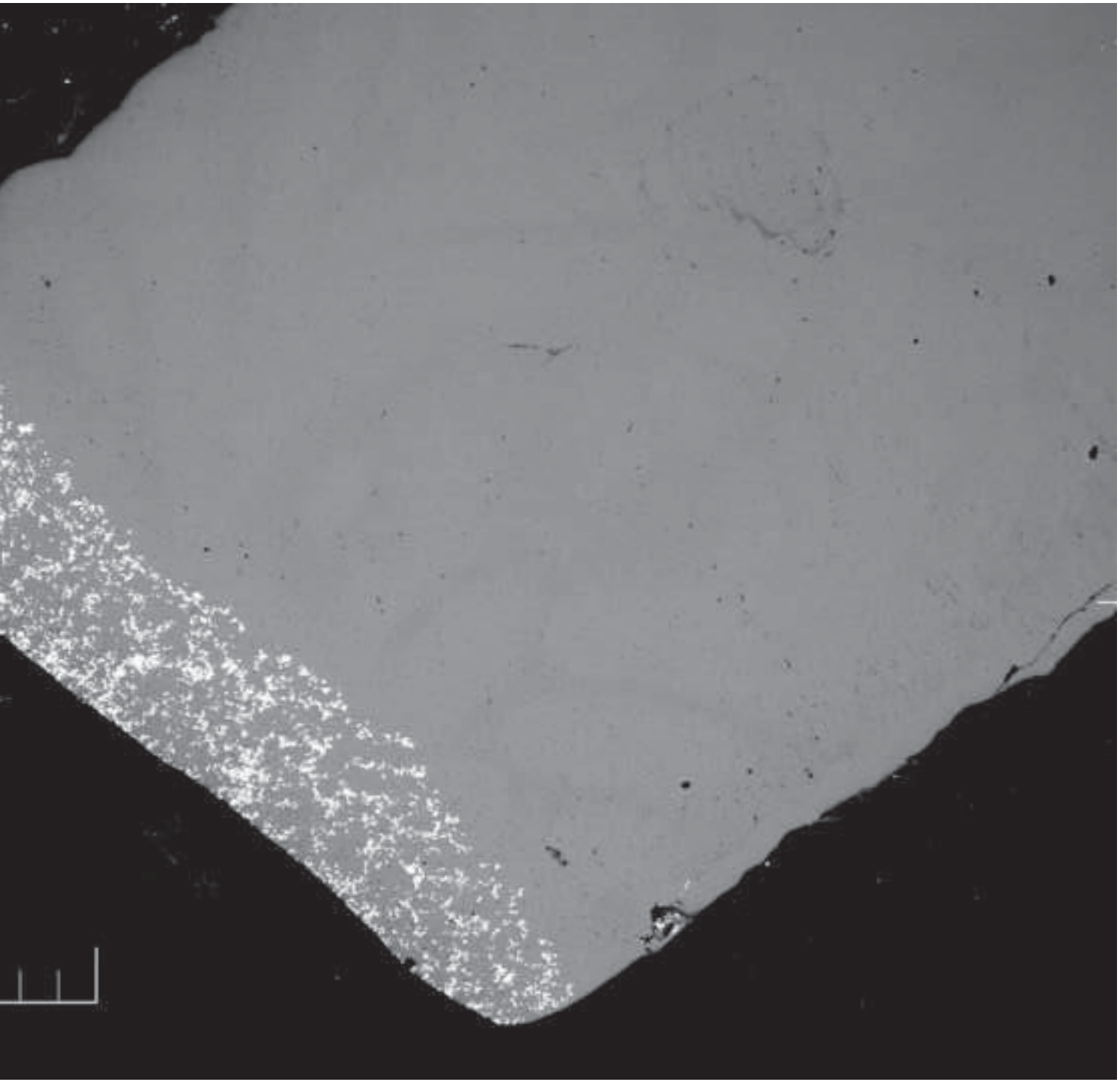

mage

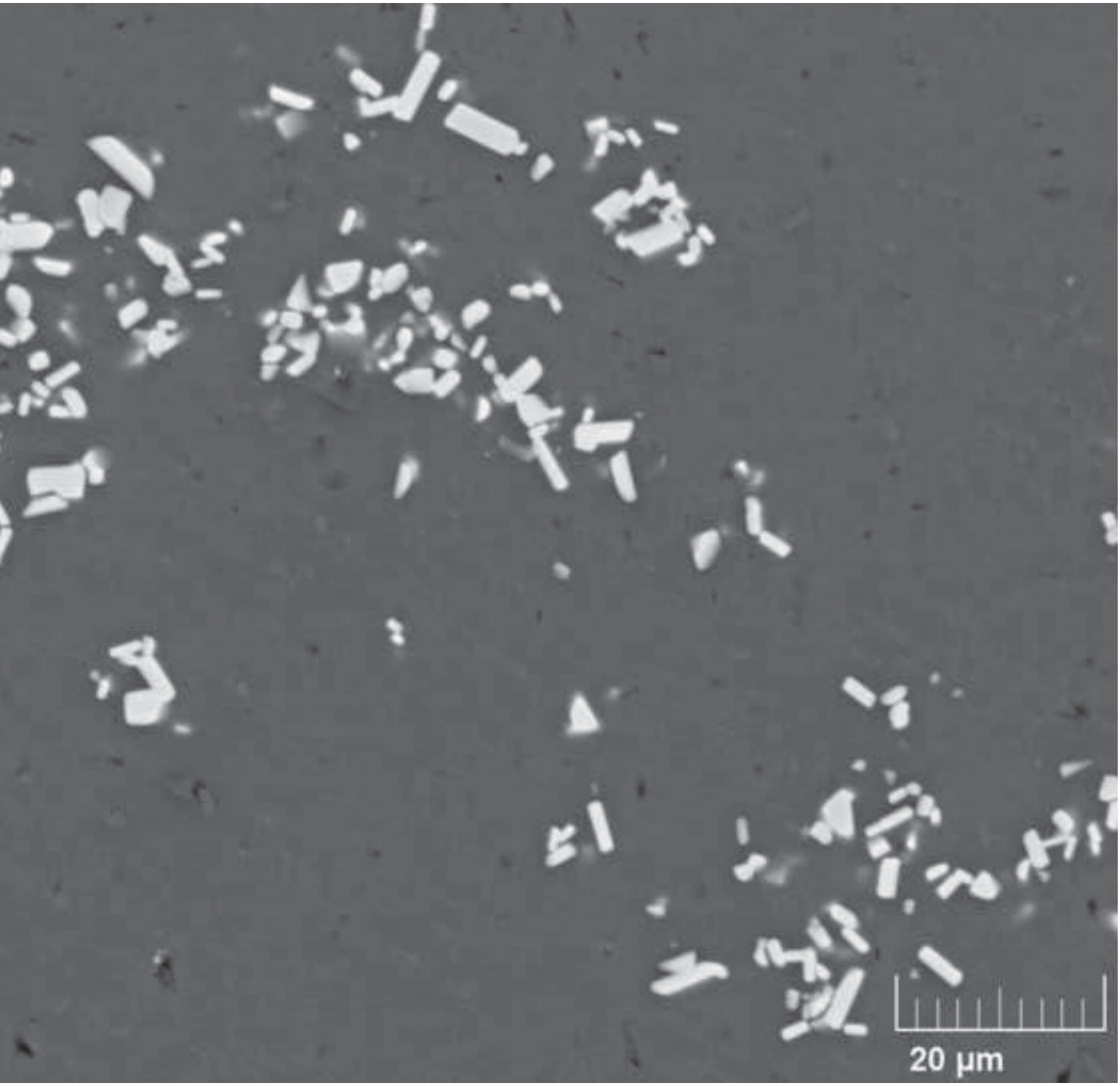

mage

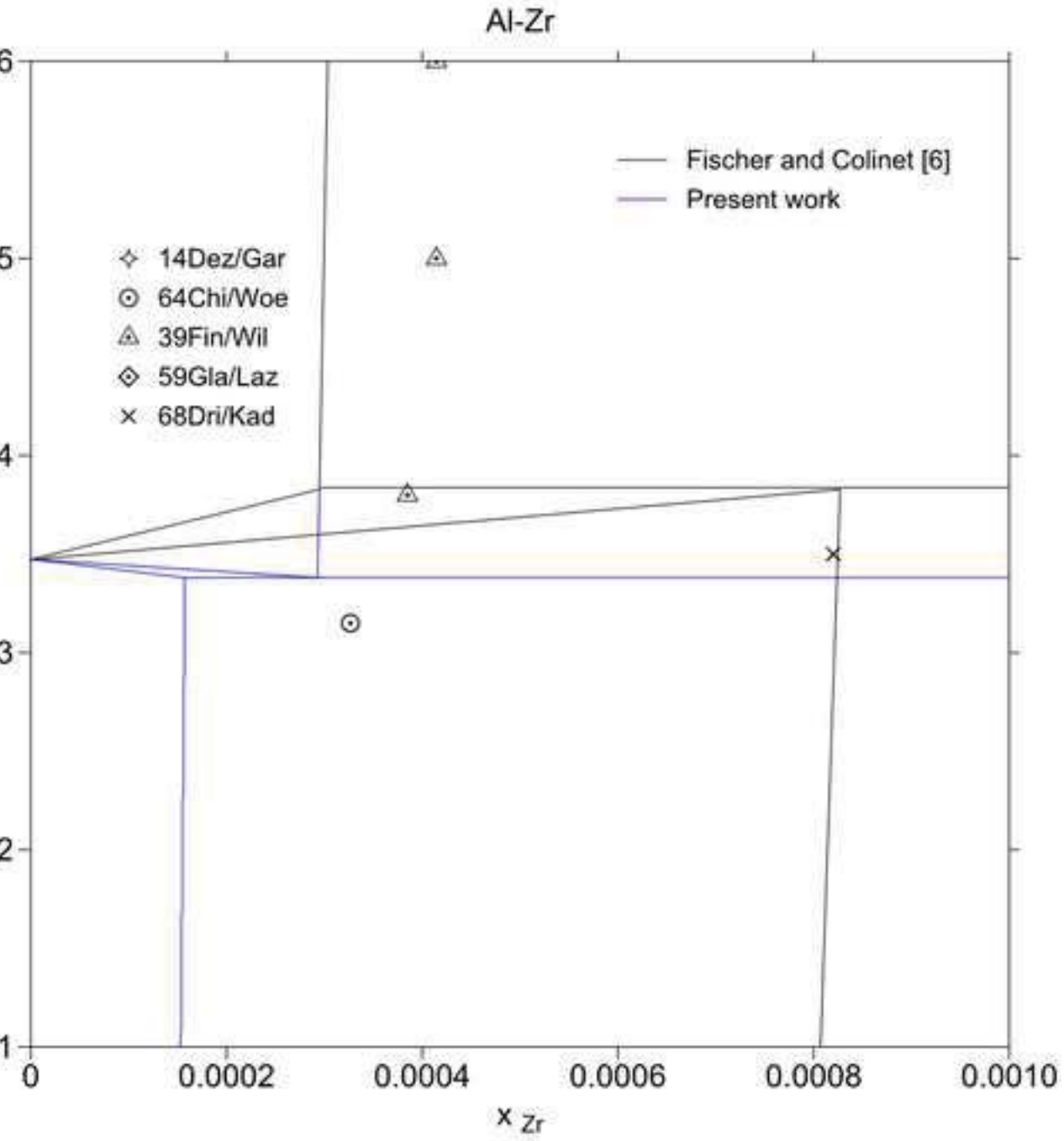
Al-Zr
Fischer and Colinet [6]
Present work
14Dez/Gar
64Chi/Woe
39Fin/Wil
59Gla/Laz
68Dri/Kad
6
5
4
3
2
1
0
0.0002
0.0004
0.0006
0.0008
0.0010
x Zr

mage

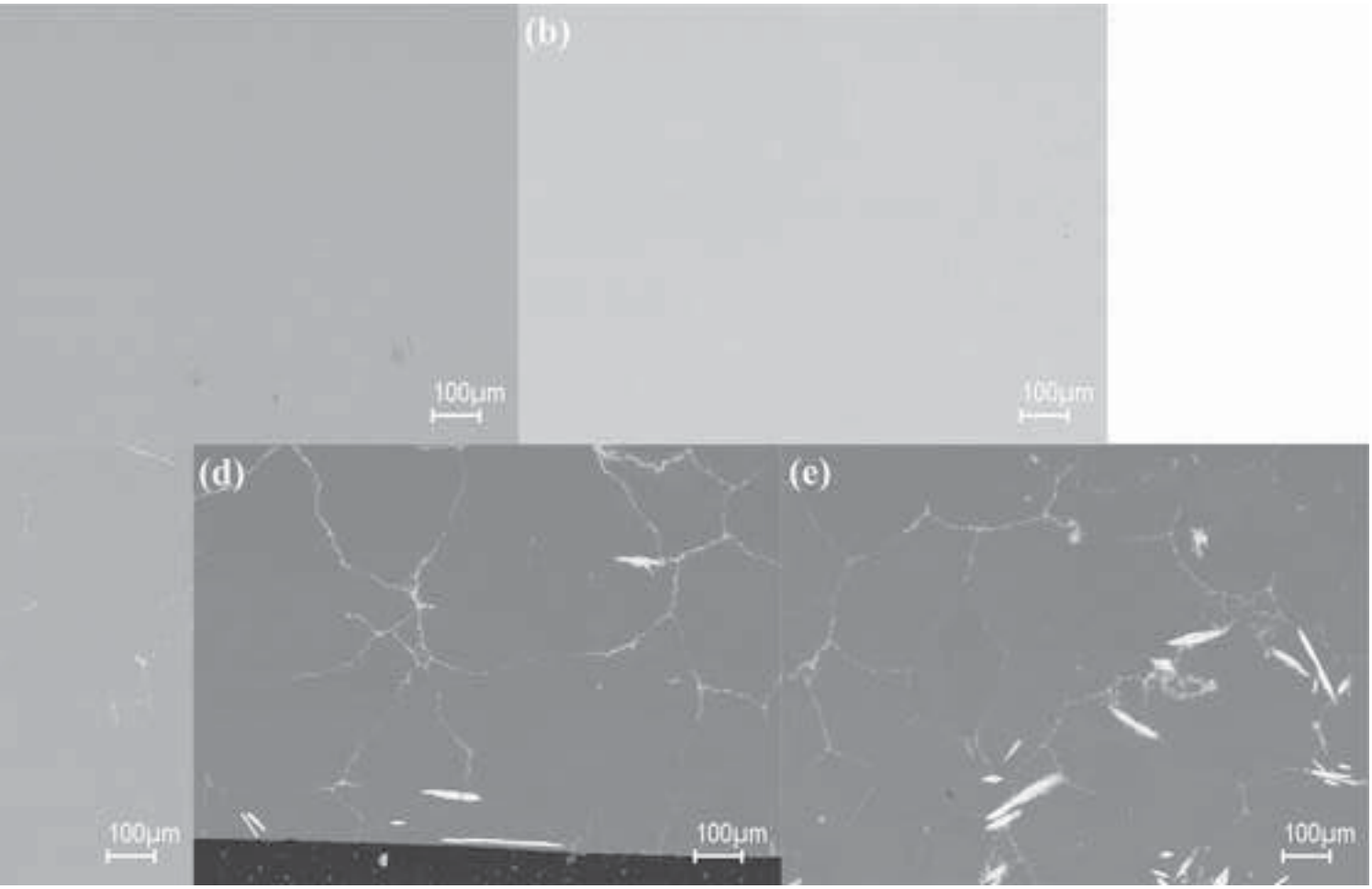

mage

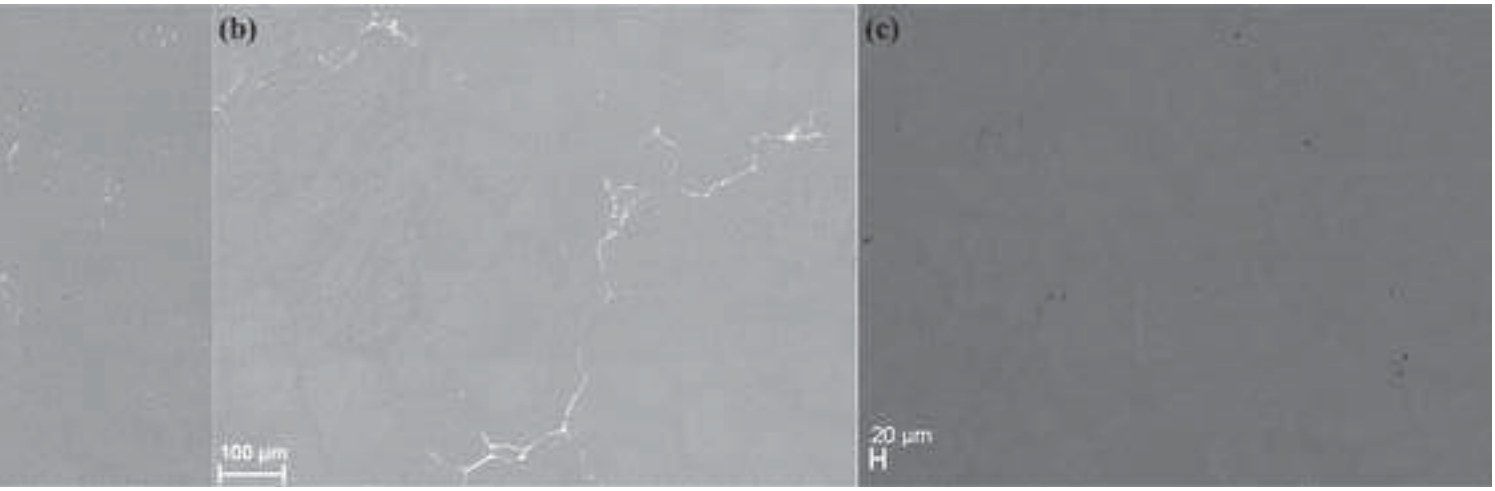

mage

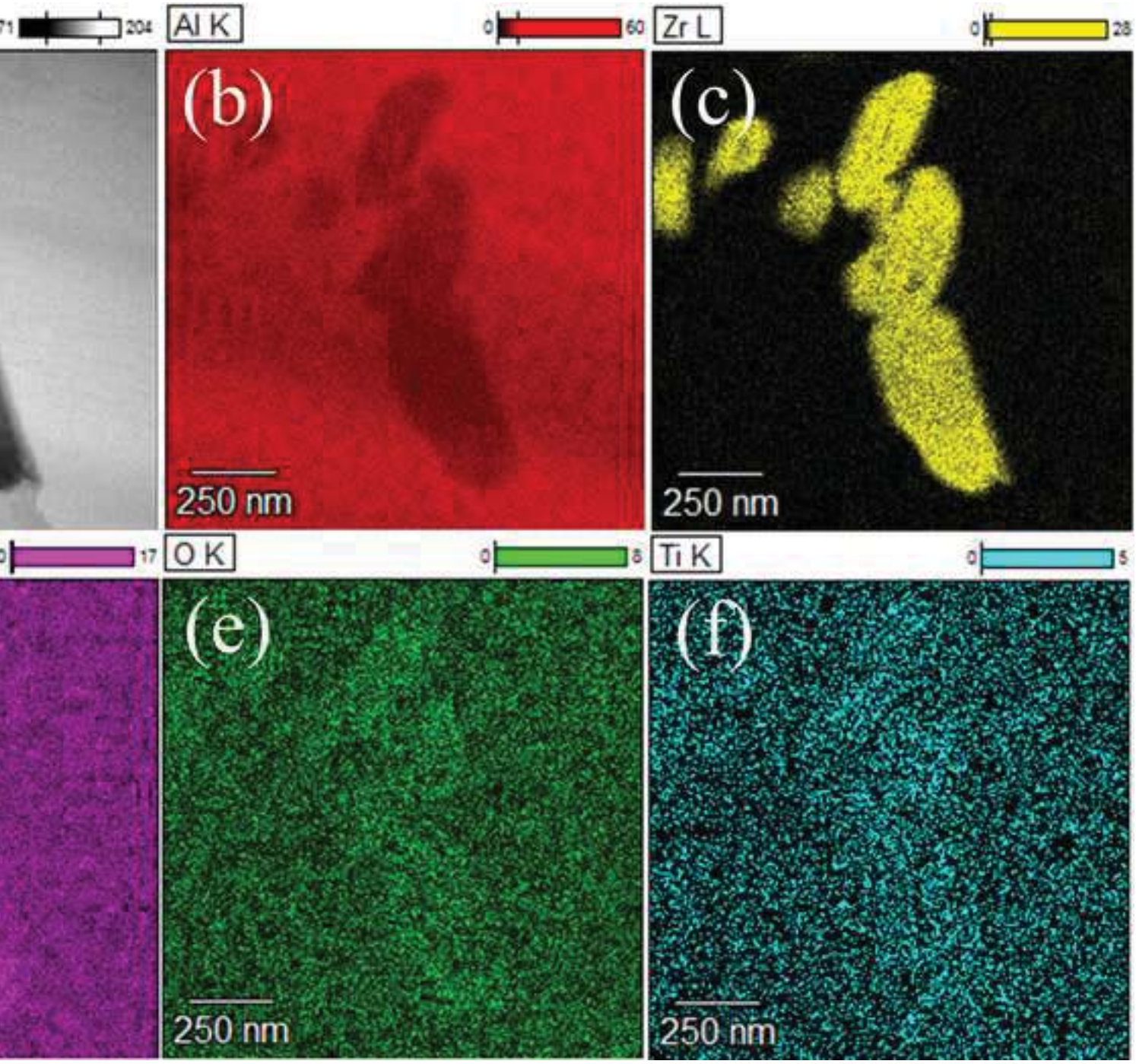
71
204
Al K
0
60
Zr L
0
28
(b)
250 nm
(c)
250 nm
0
17
O K
0
8
Ti K
0
5
(e)
250 nm
(f)
250 nm

mage

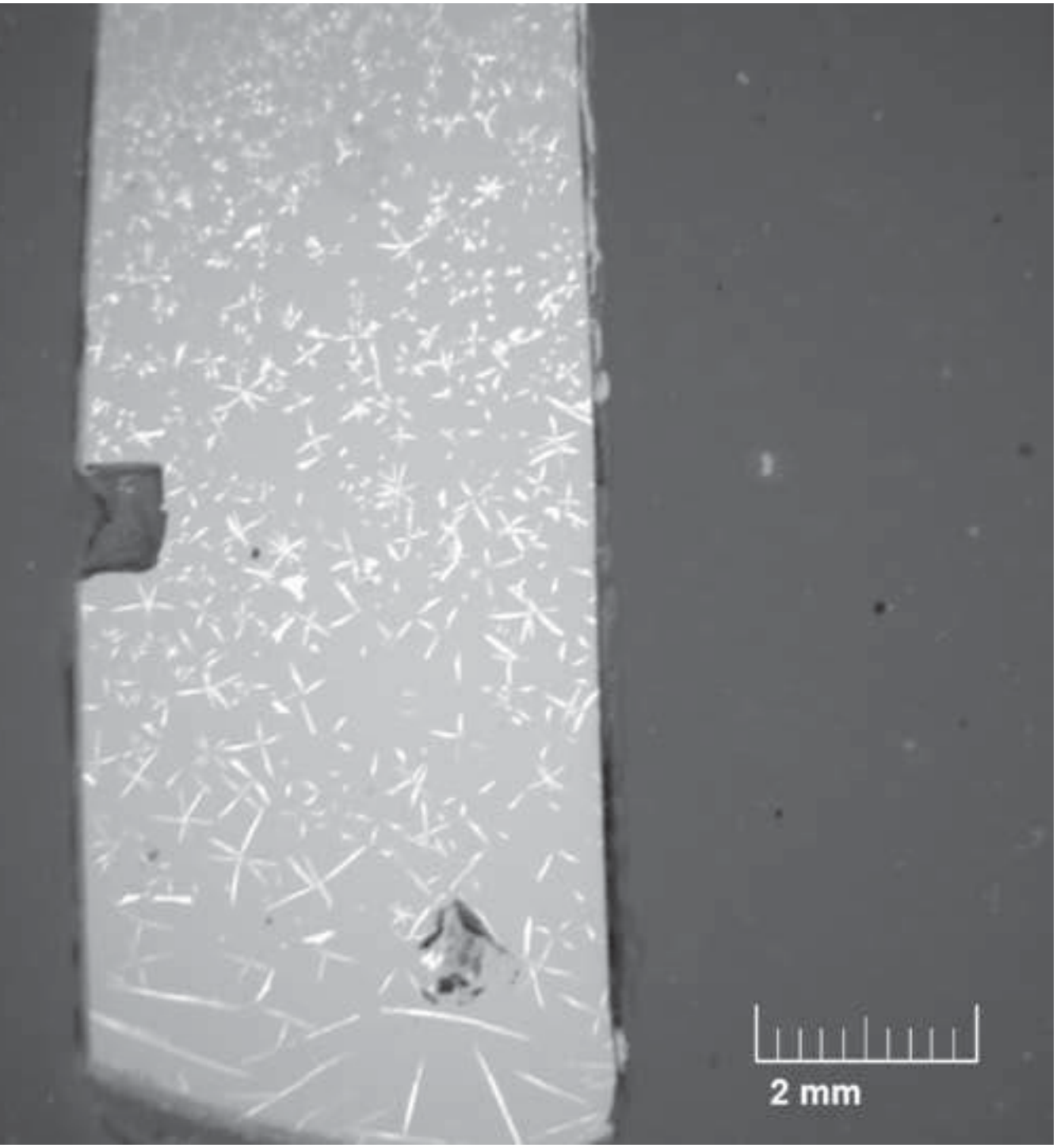

mage

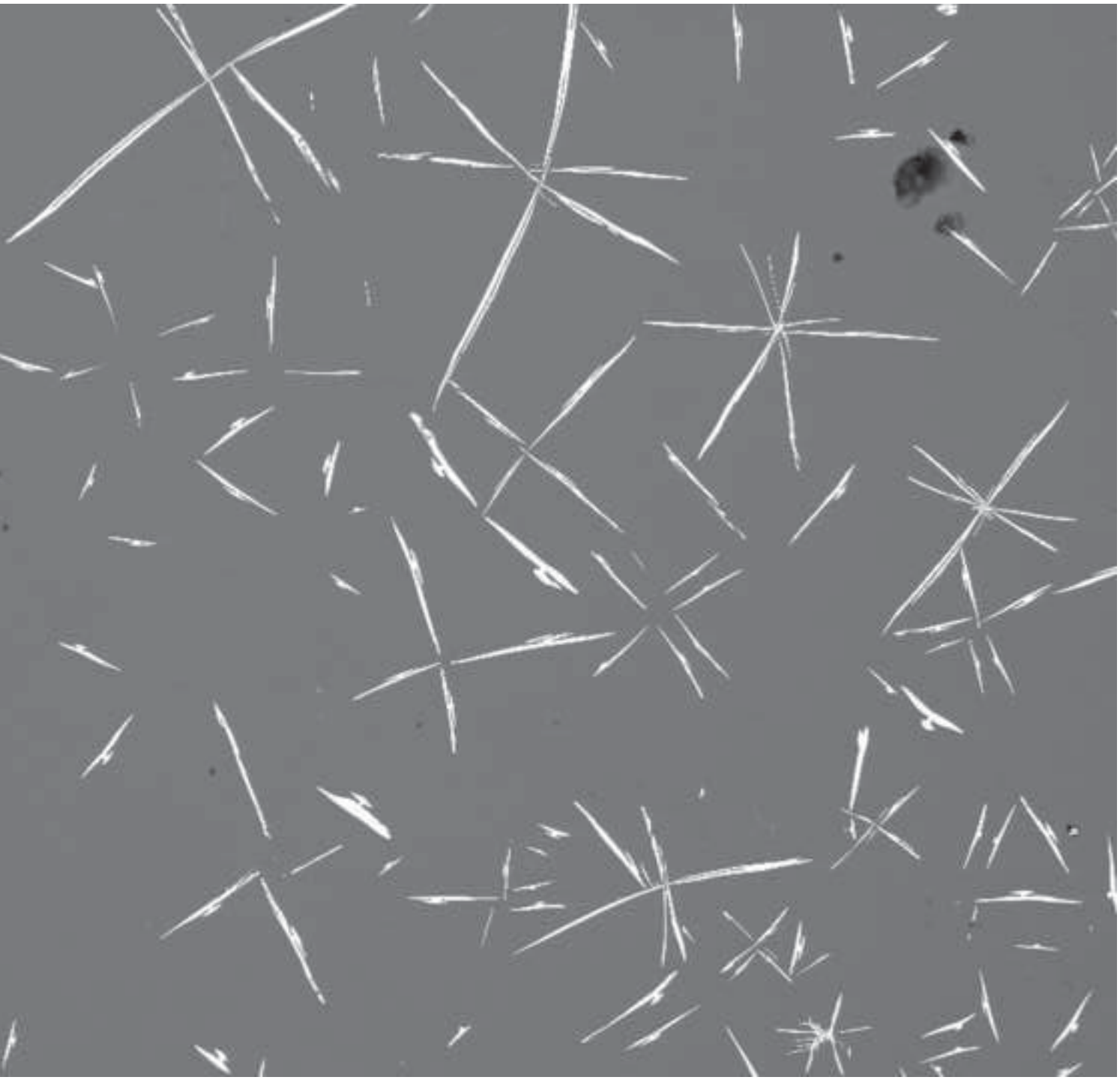

mage

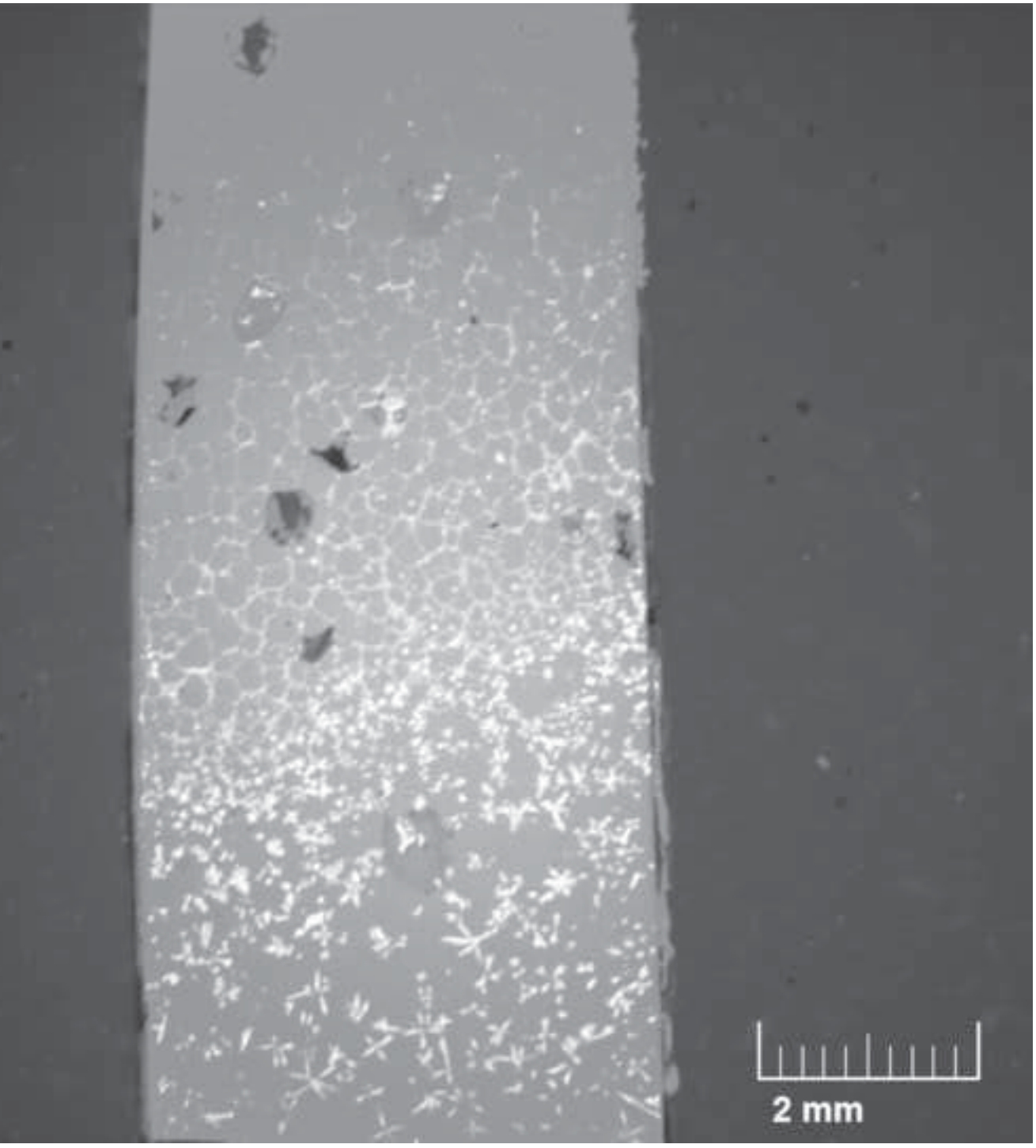

mage

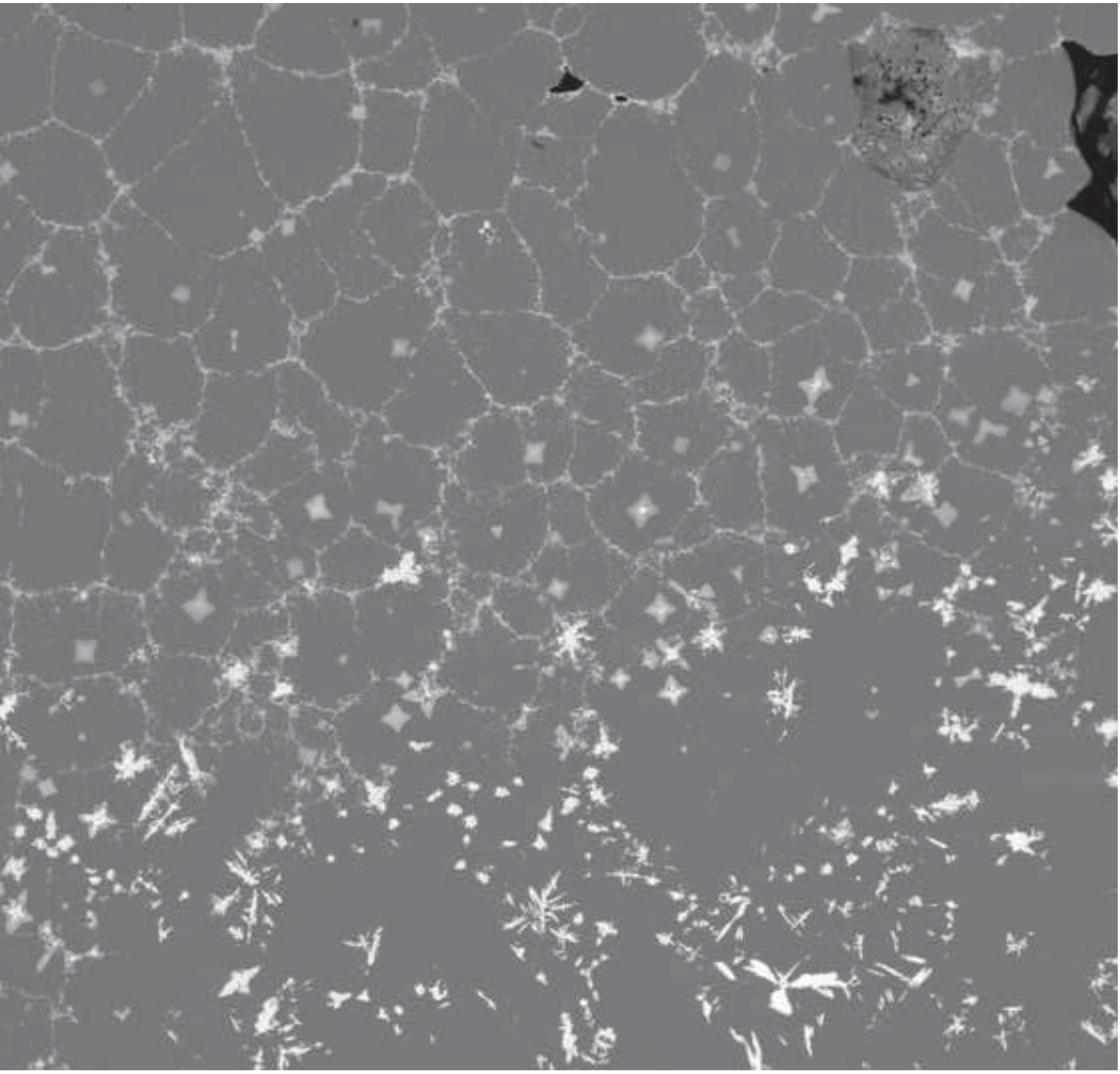

mage

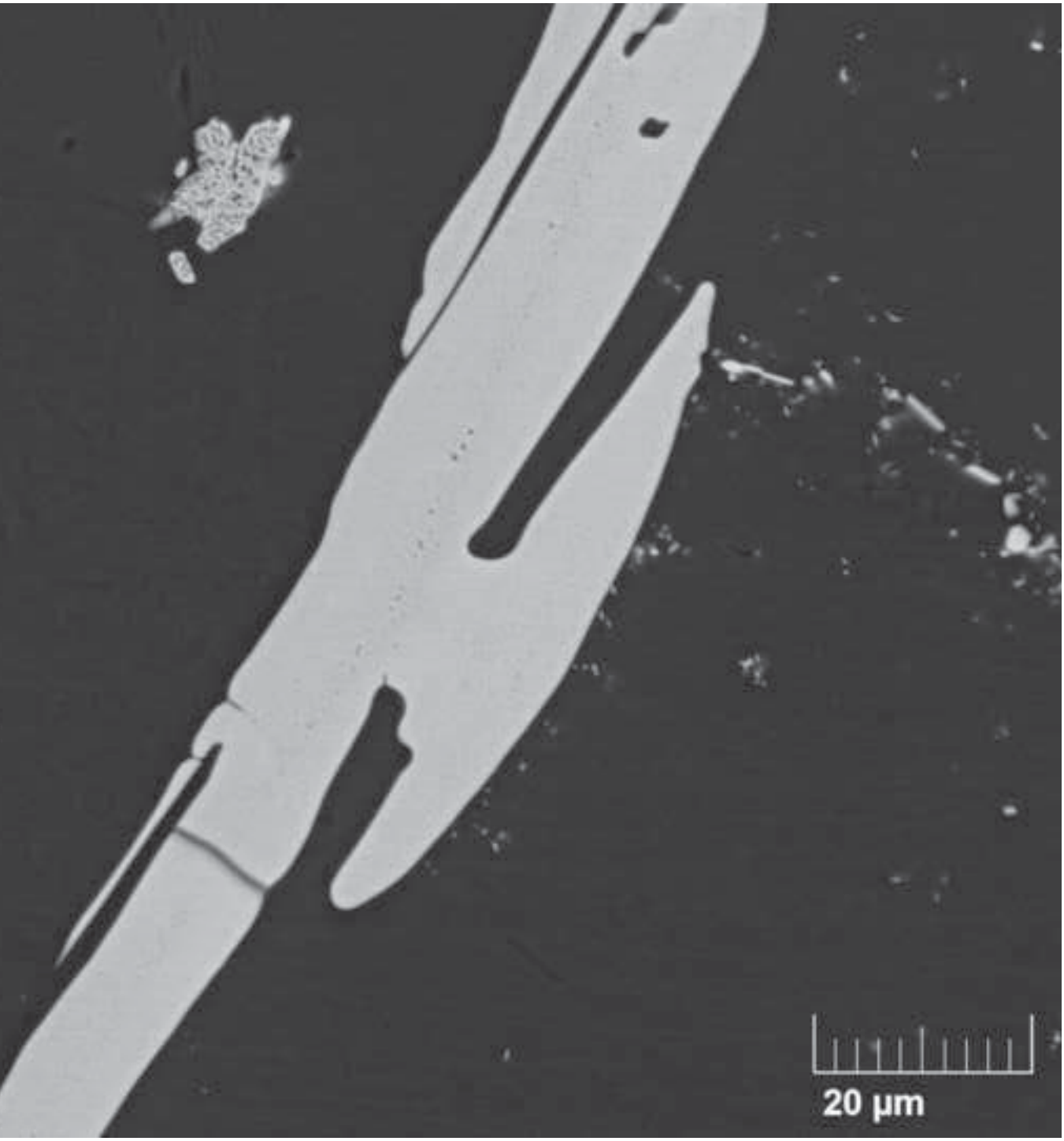

mage

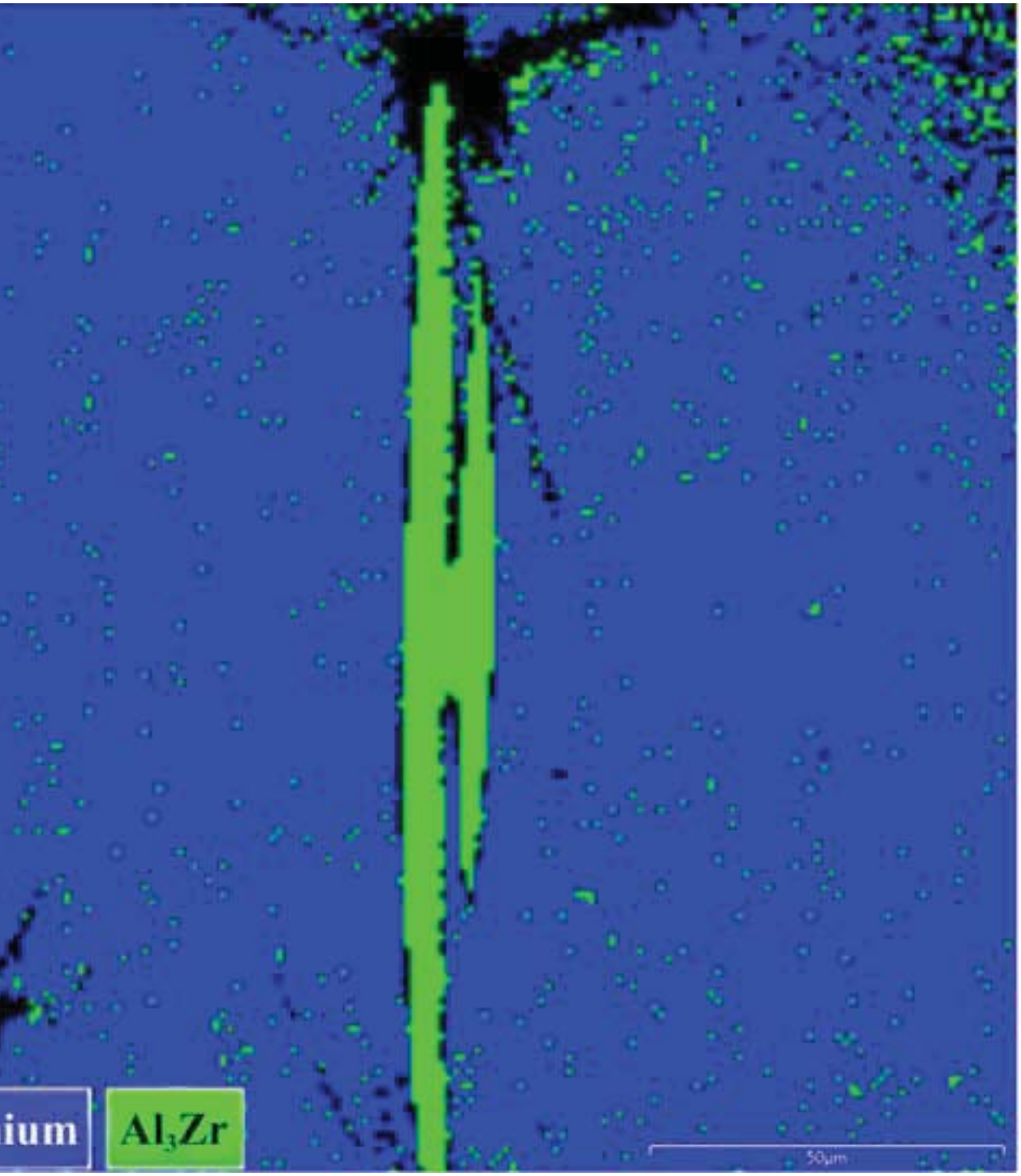

mage

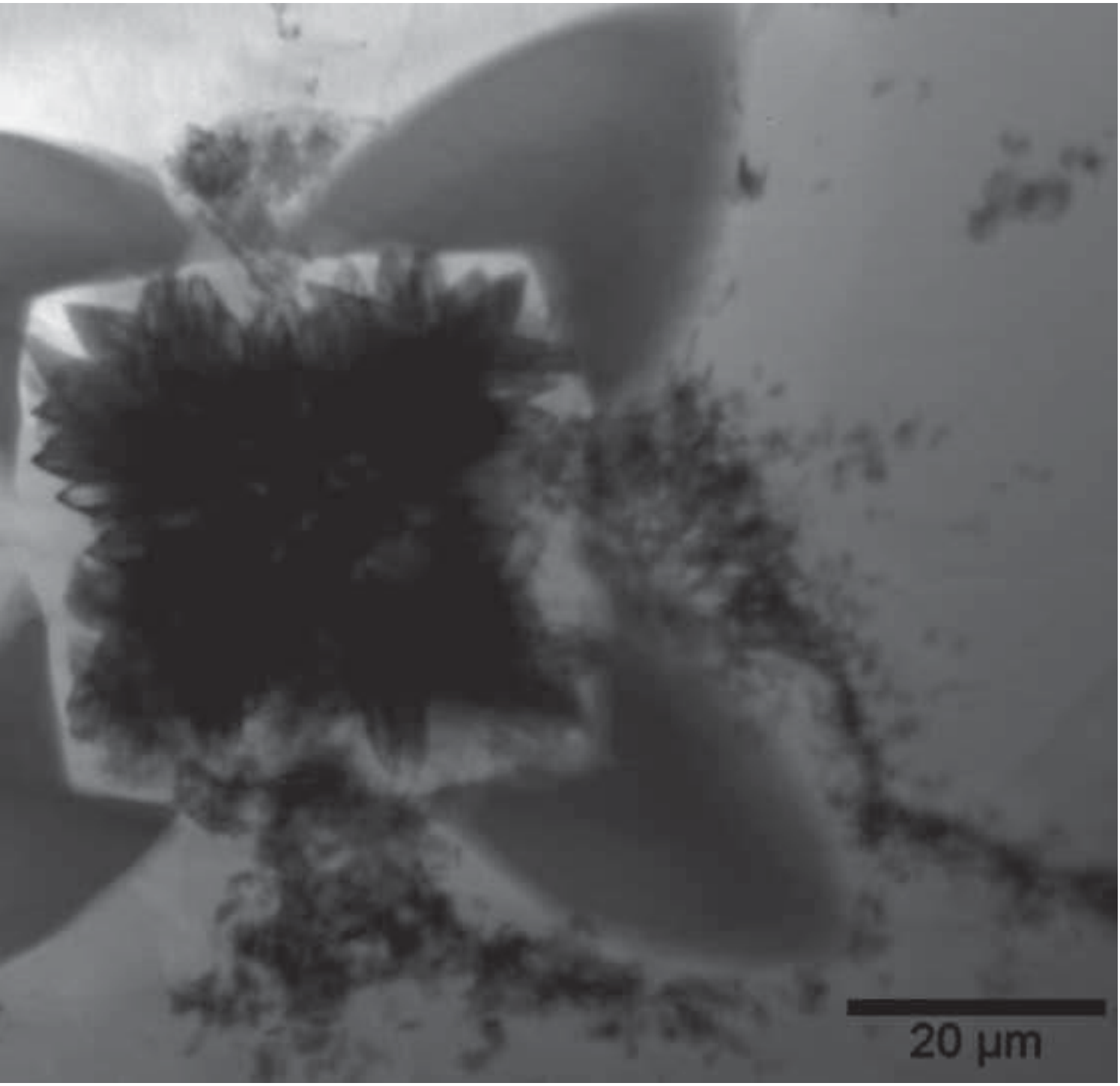

mage

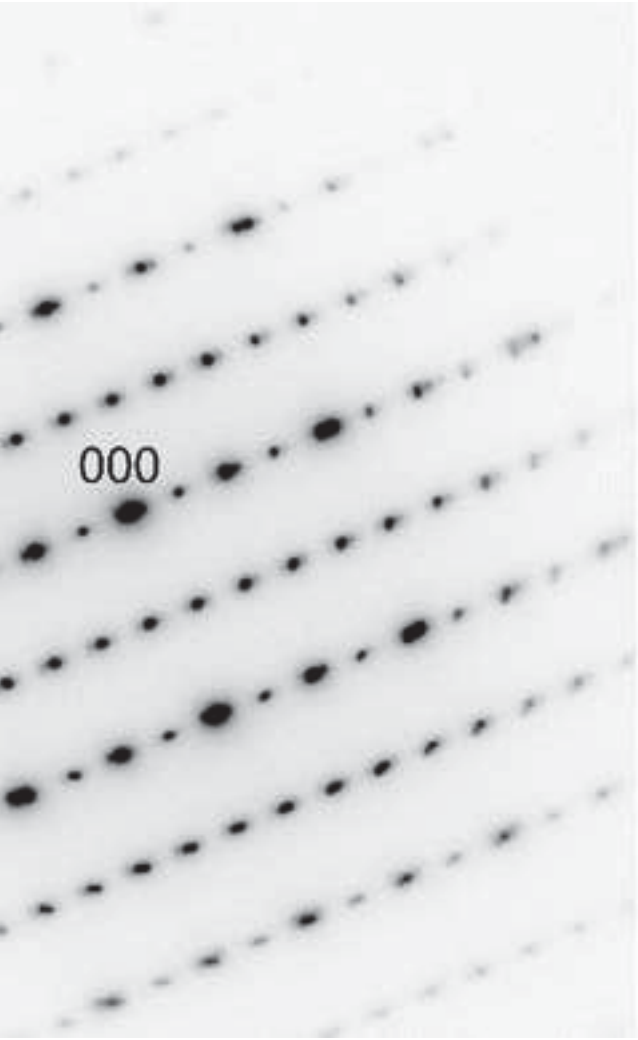

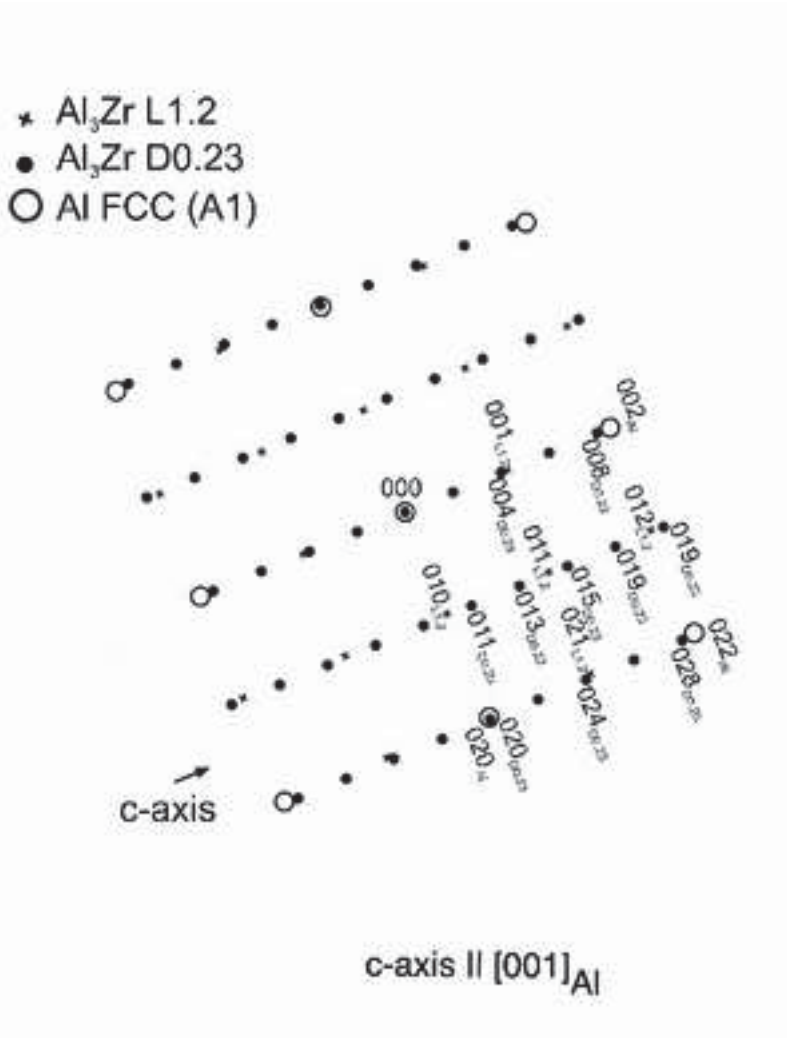

mage

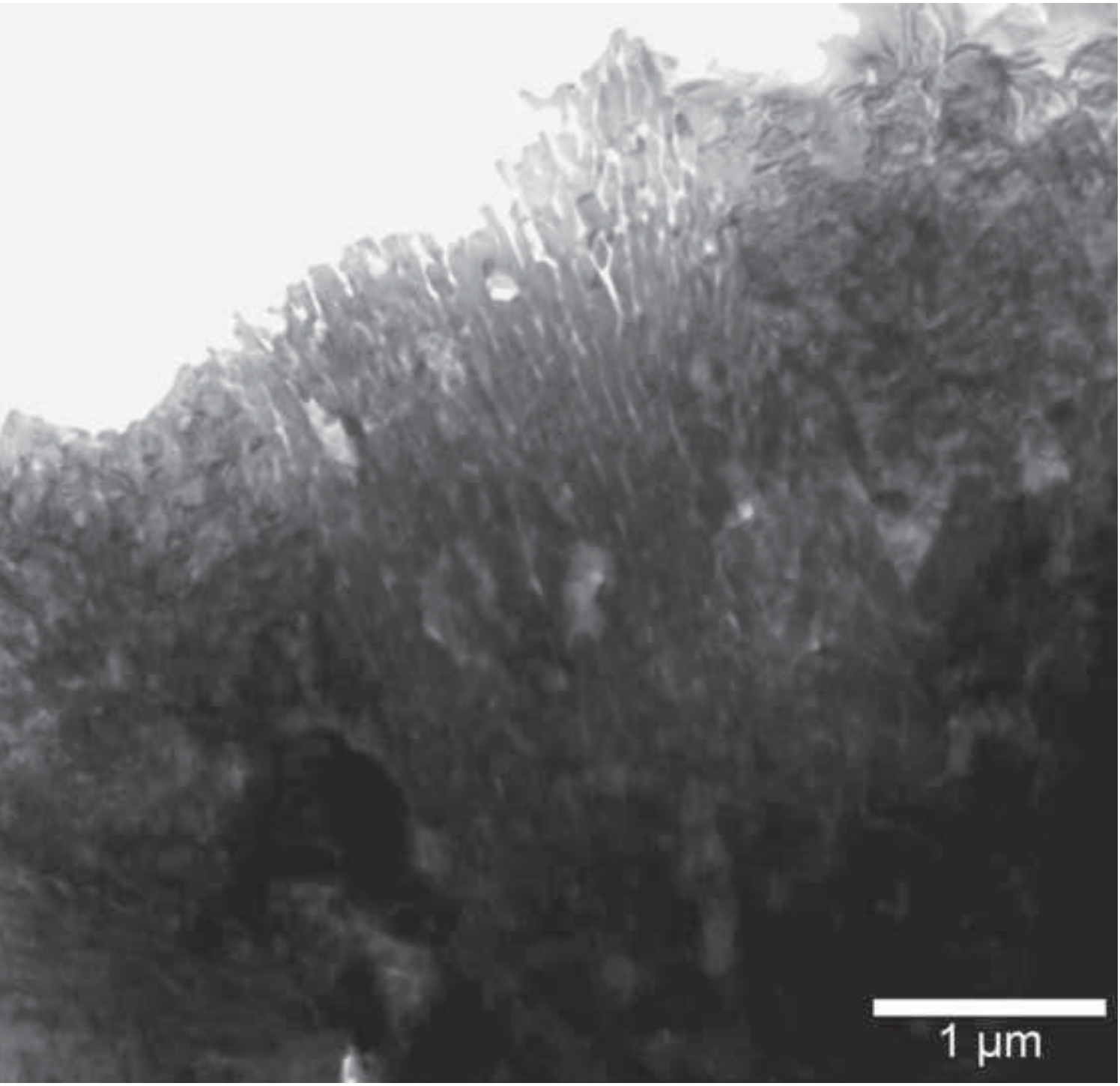

mage

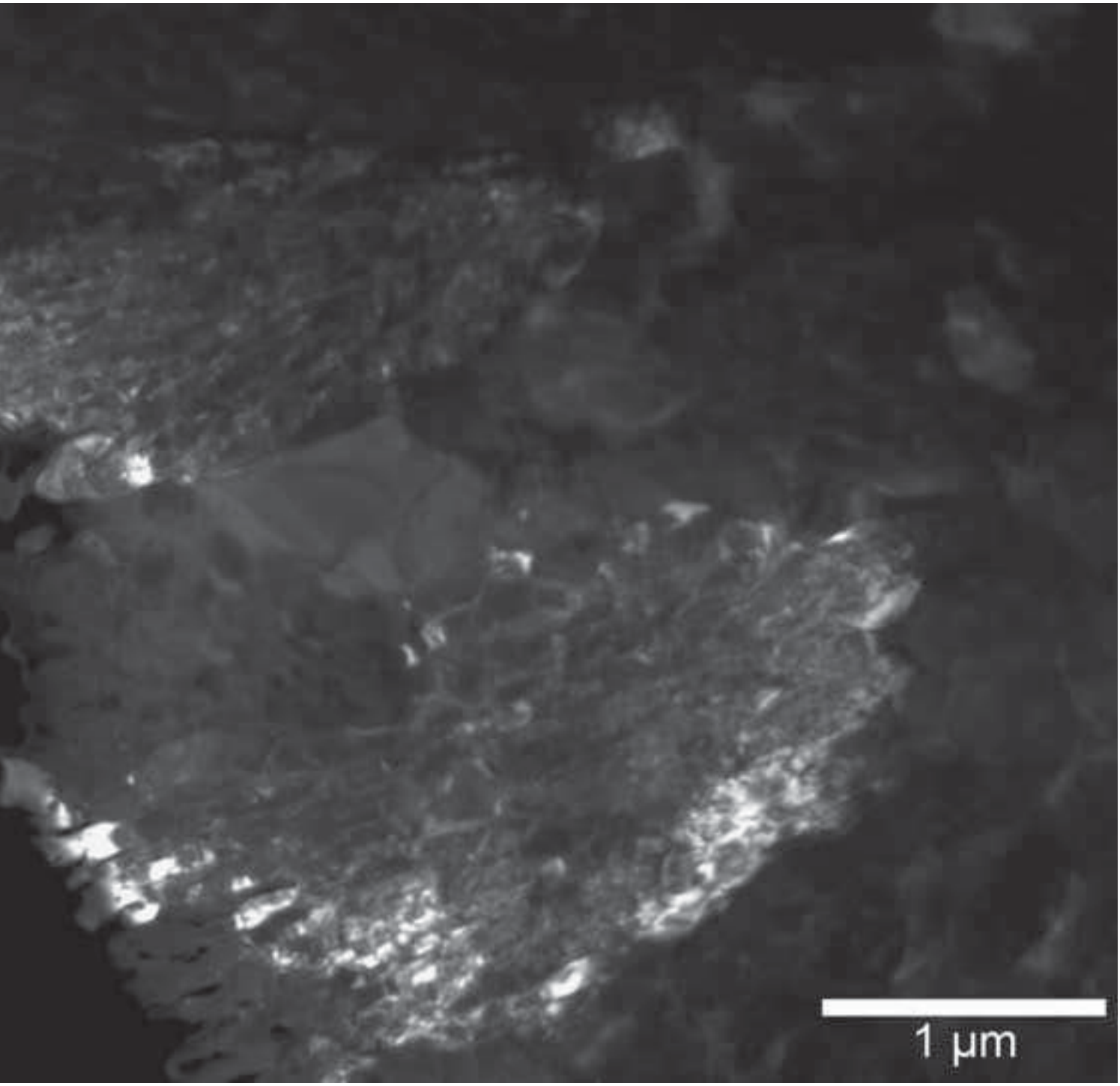

mage

mage

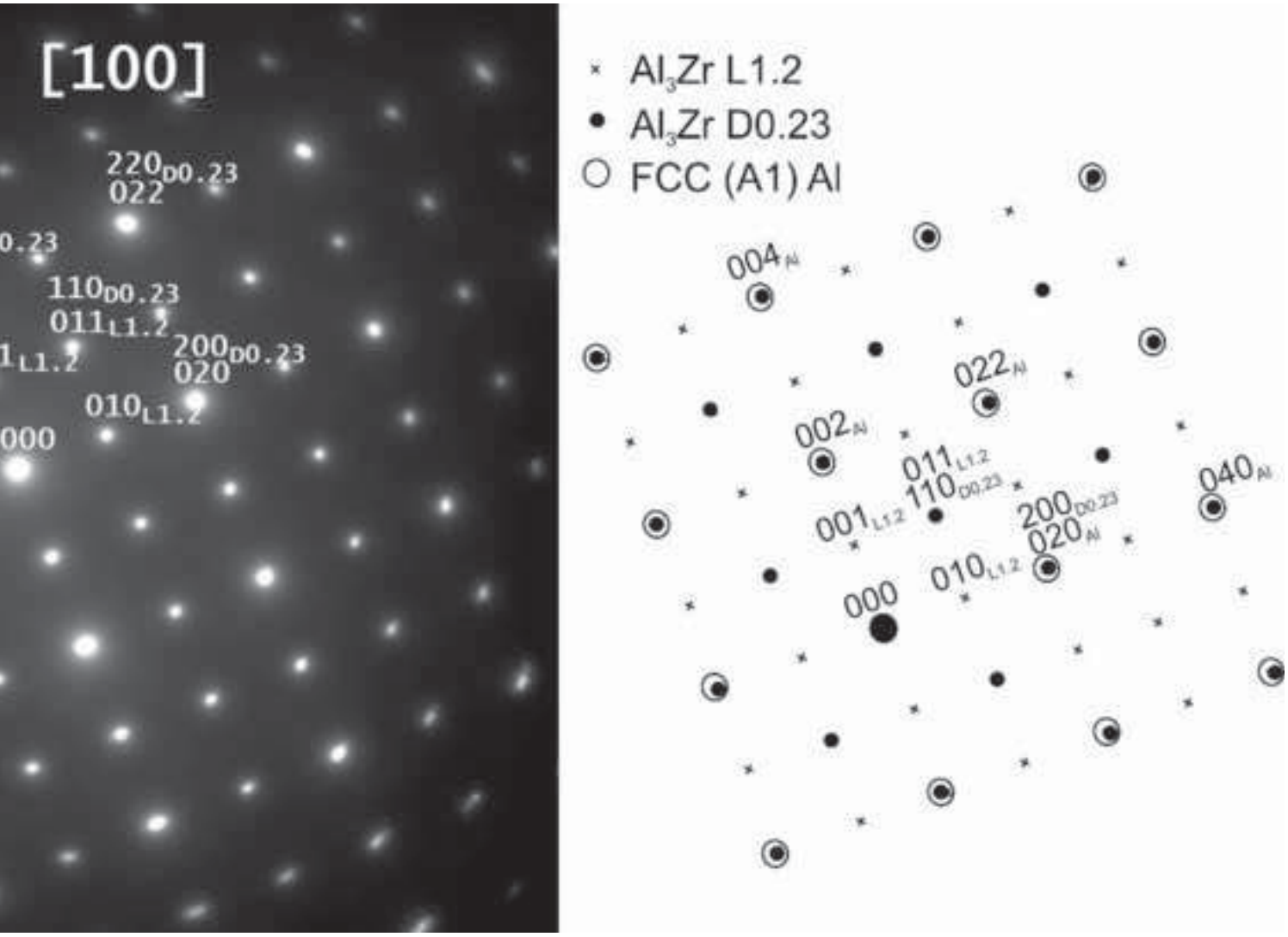
[100]
220D0.23
022
0.23
110D0.23
011L1.2
1L1.2
200D0.23
020
010L1.2
000
Al3Zr L1.2
Al3Zr D0.23
FCC (A1) Al
004Al
022Al
002Al
011L1.2
110D0.23
001L1.2
200D0.23
020Al
040Al
010L1.2
000

Figure 12-a

Click here to download high resolution image

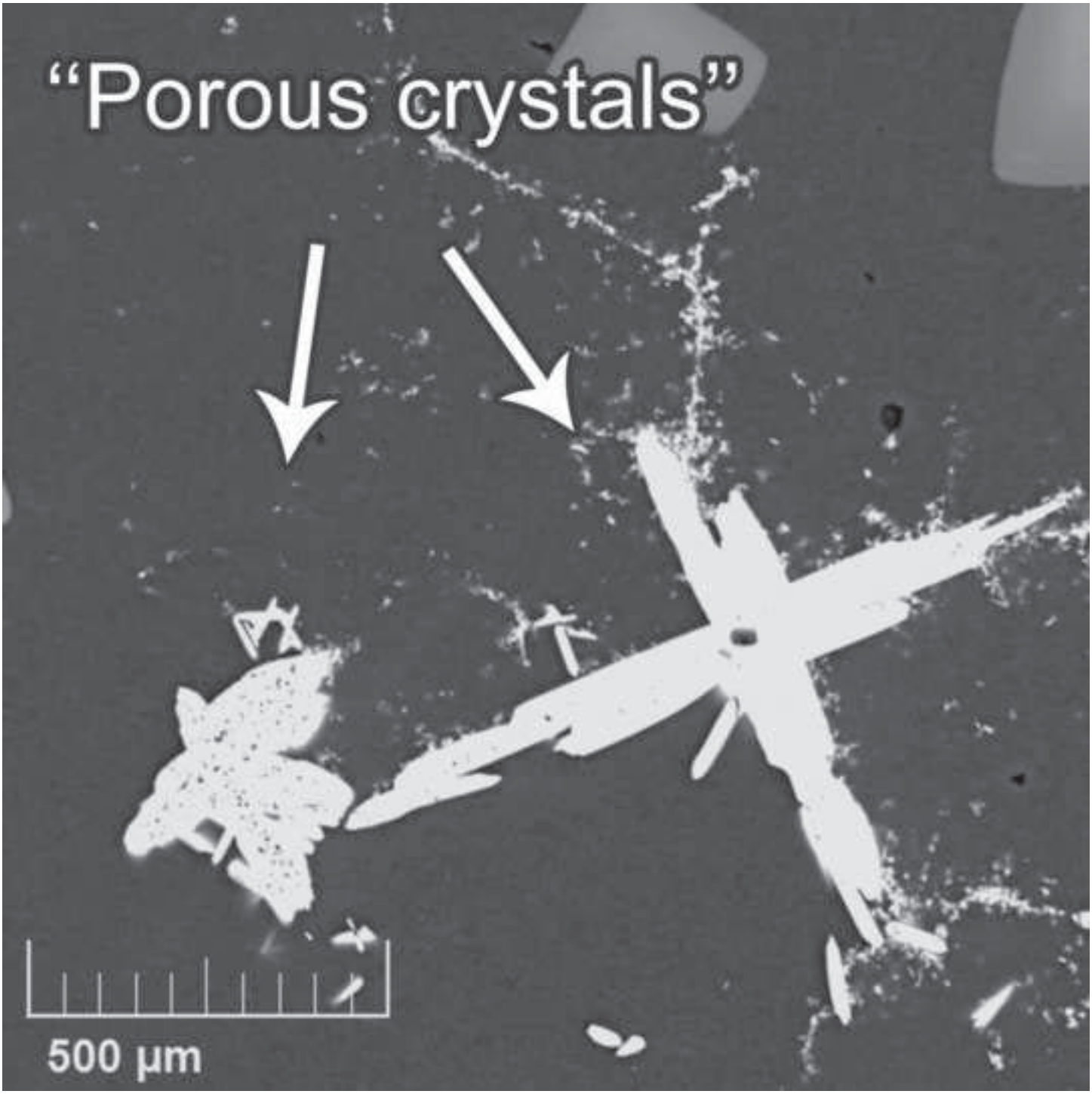

Figure 12-b

Click here to download high resolution image

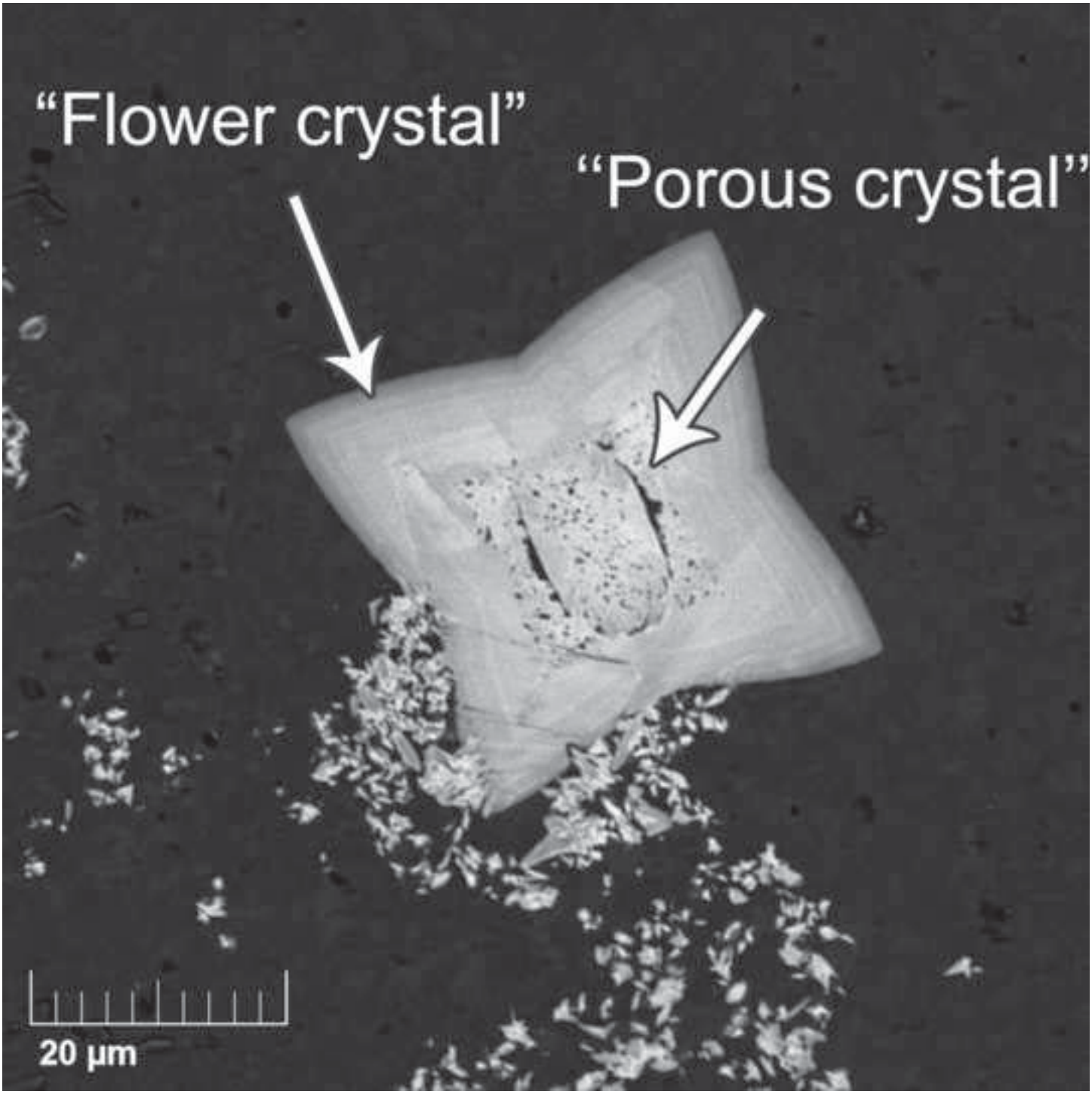

mage

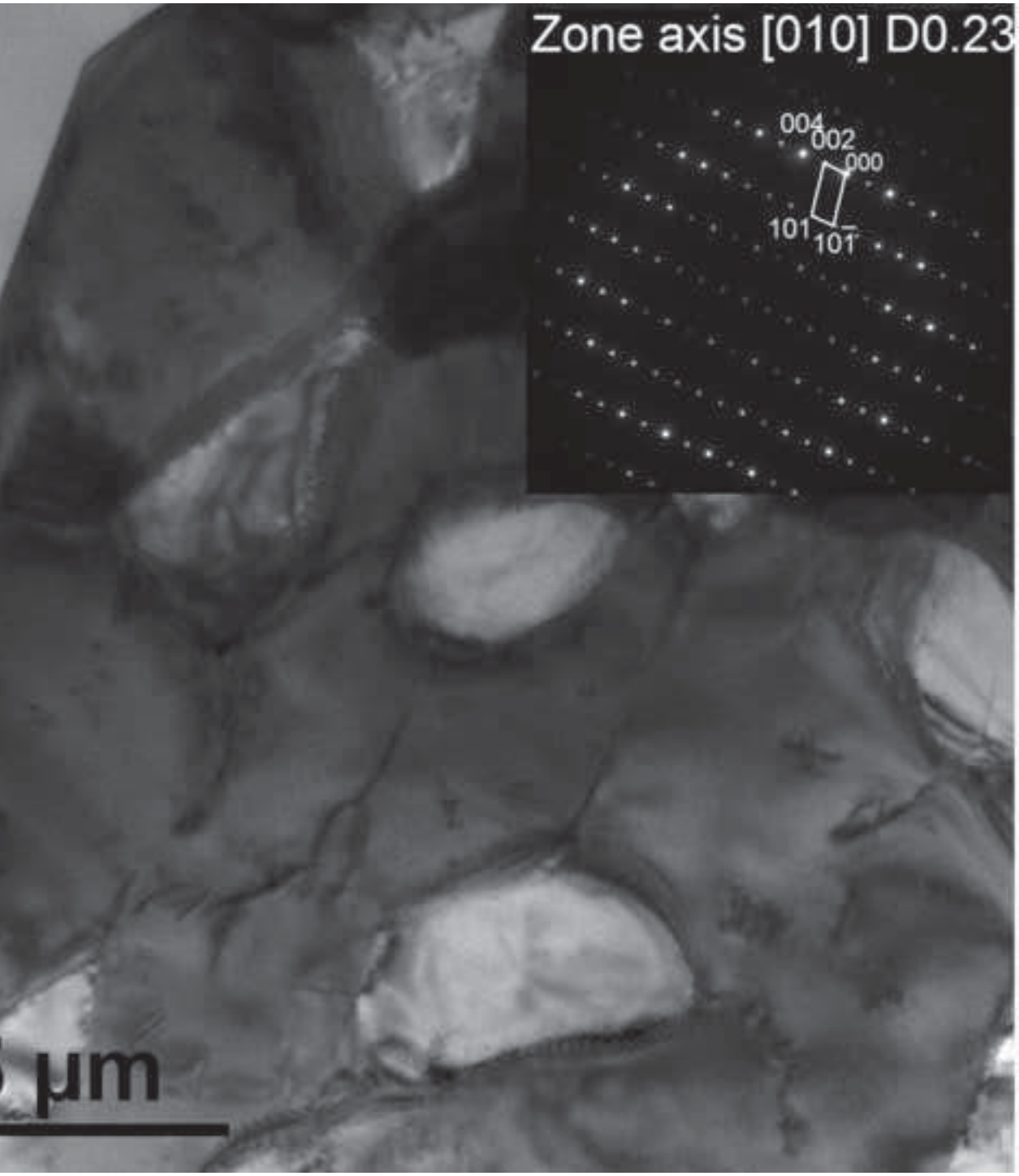

mage

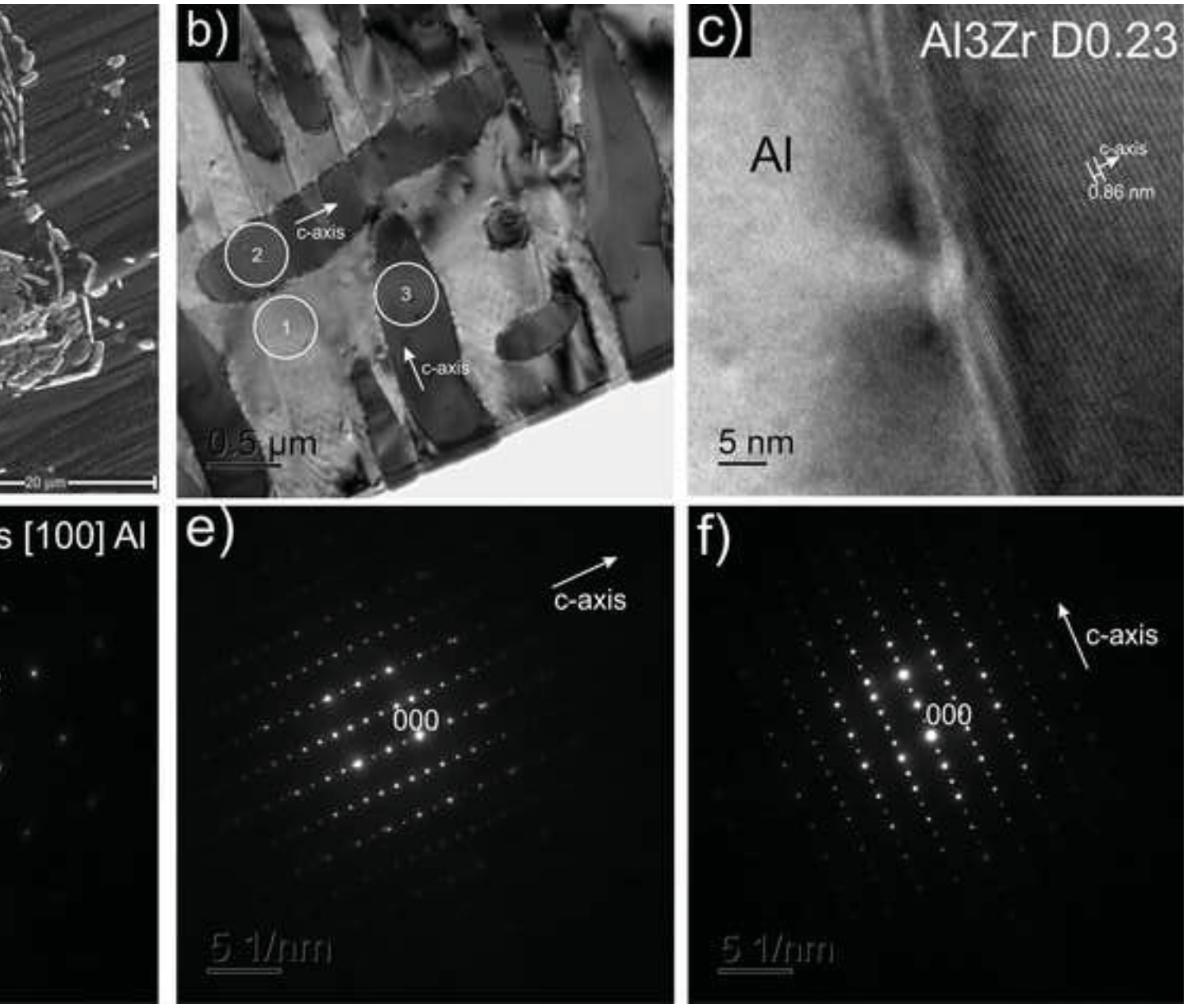
b)
c-axis
2
3
1
c-axis
0.5 μm
c)
Al3Zr D0.23
Al
c-axis
0.86 nm
5 nm
s [100] Al
e)
c-axis
000
5 1/nm
f)
c-axis
000
5 1/nm

Figure 14-a

Click here to download high resolution image

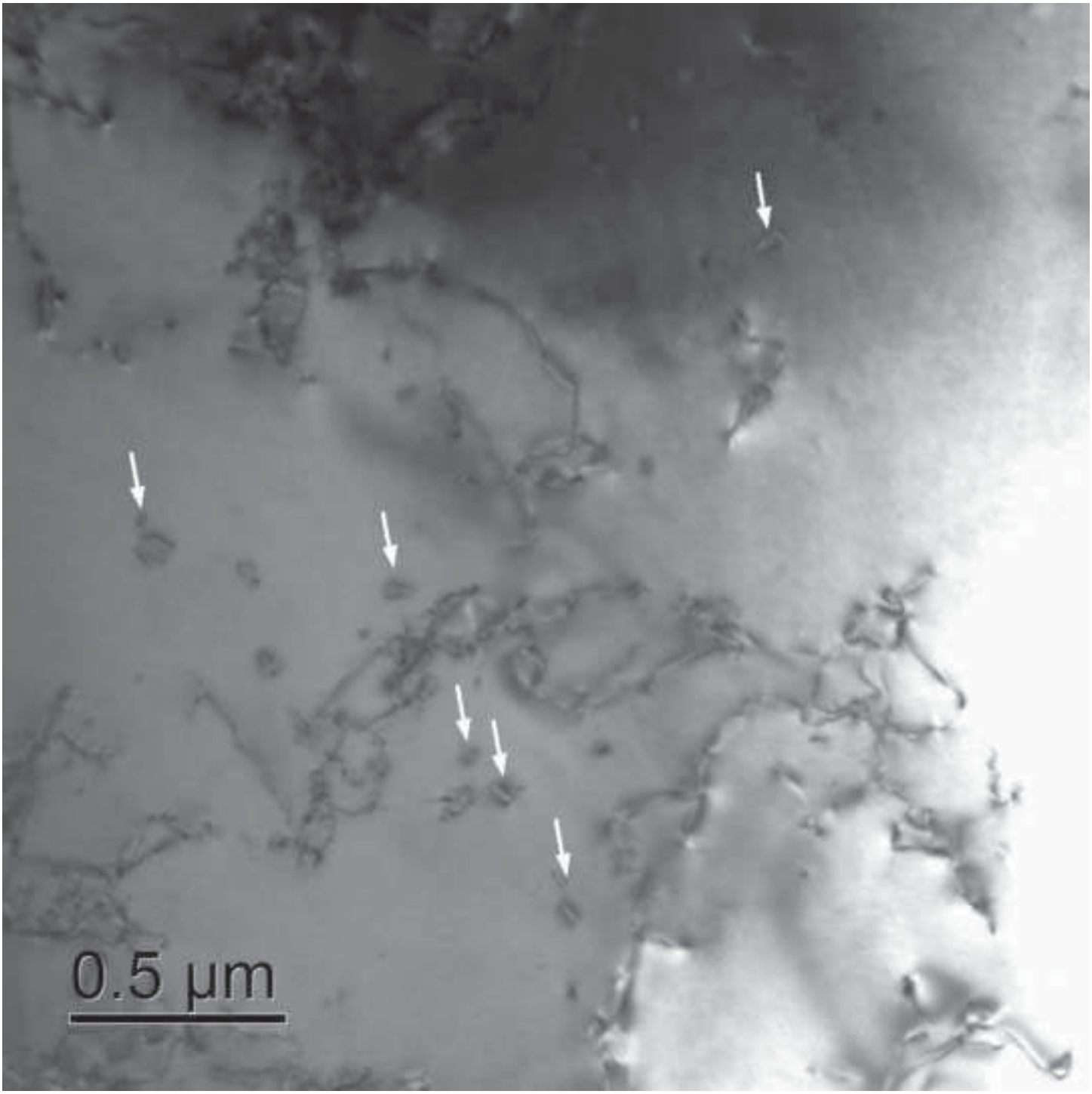

Figure 14-b

Click here to download high resolution image

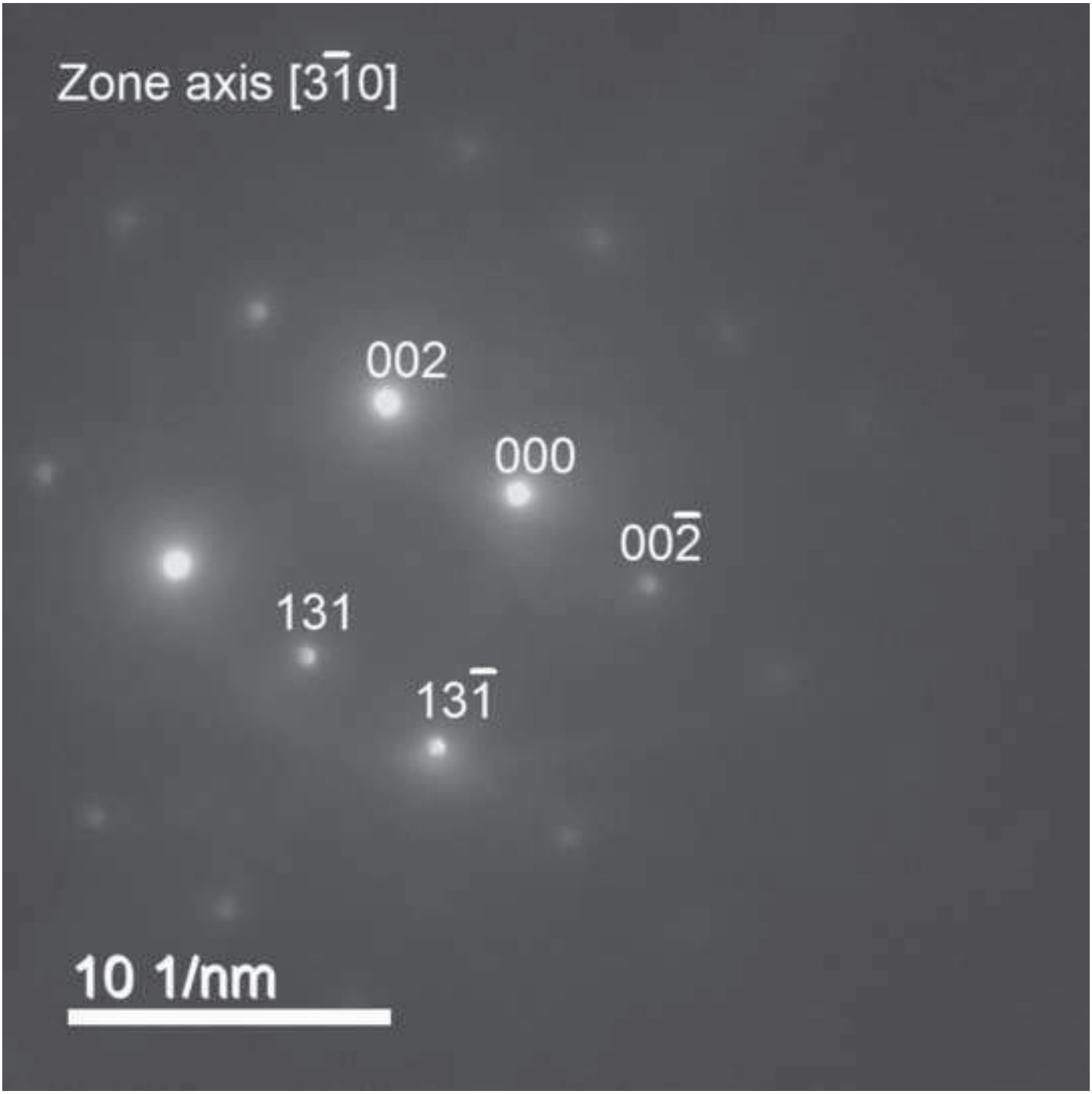

mage

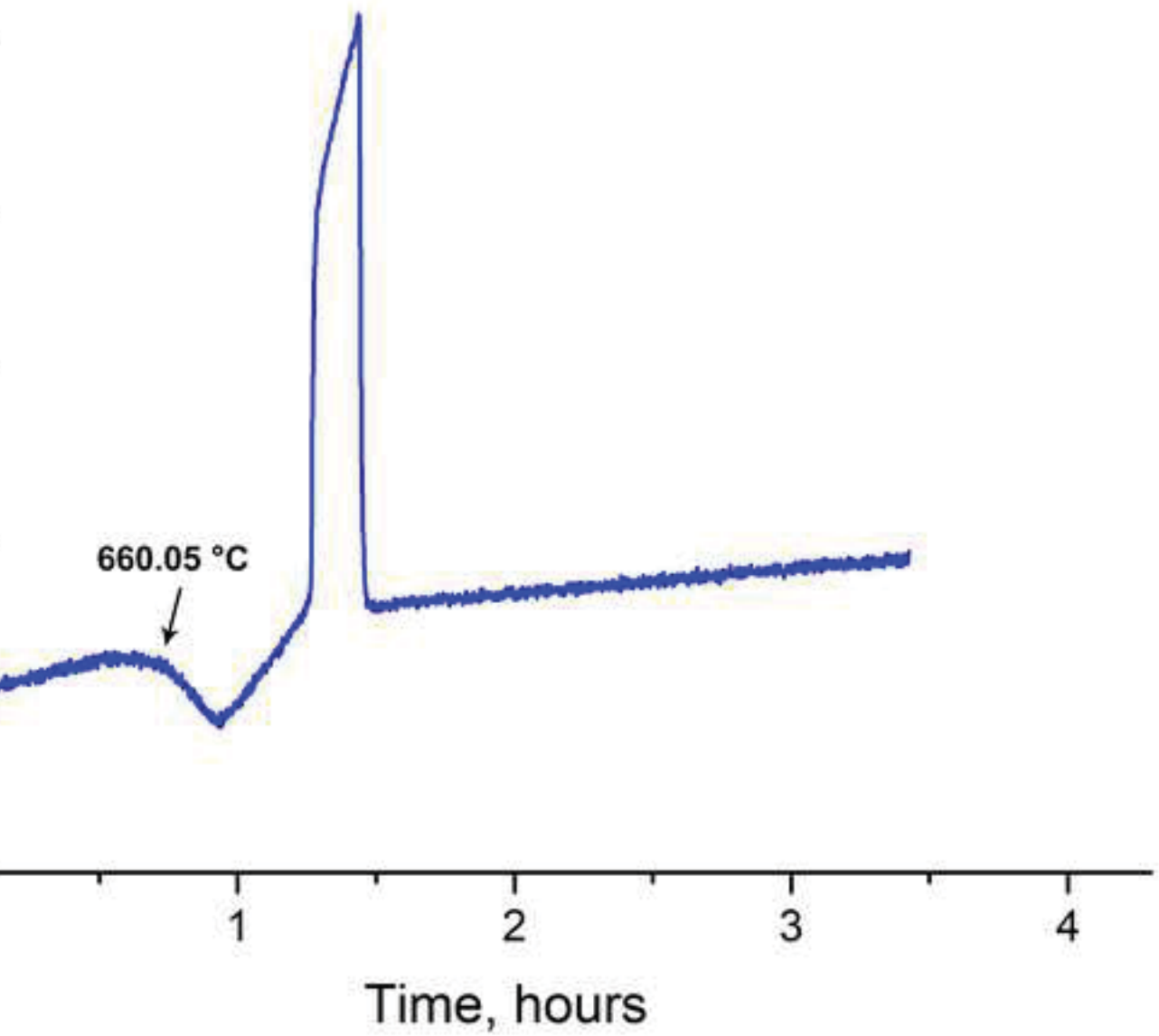

mage

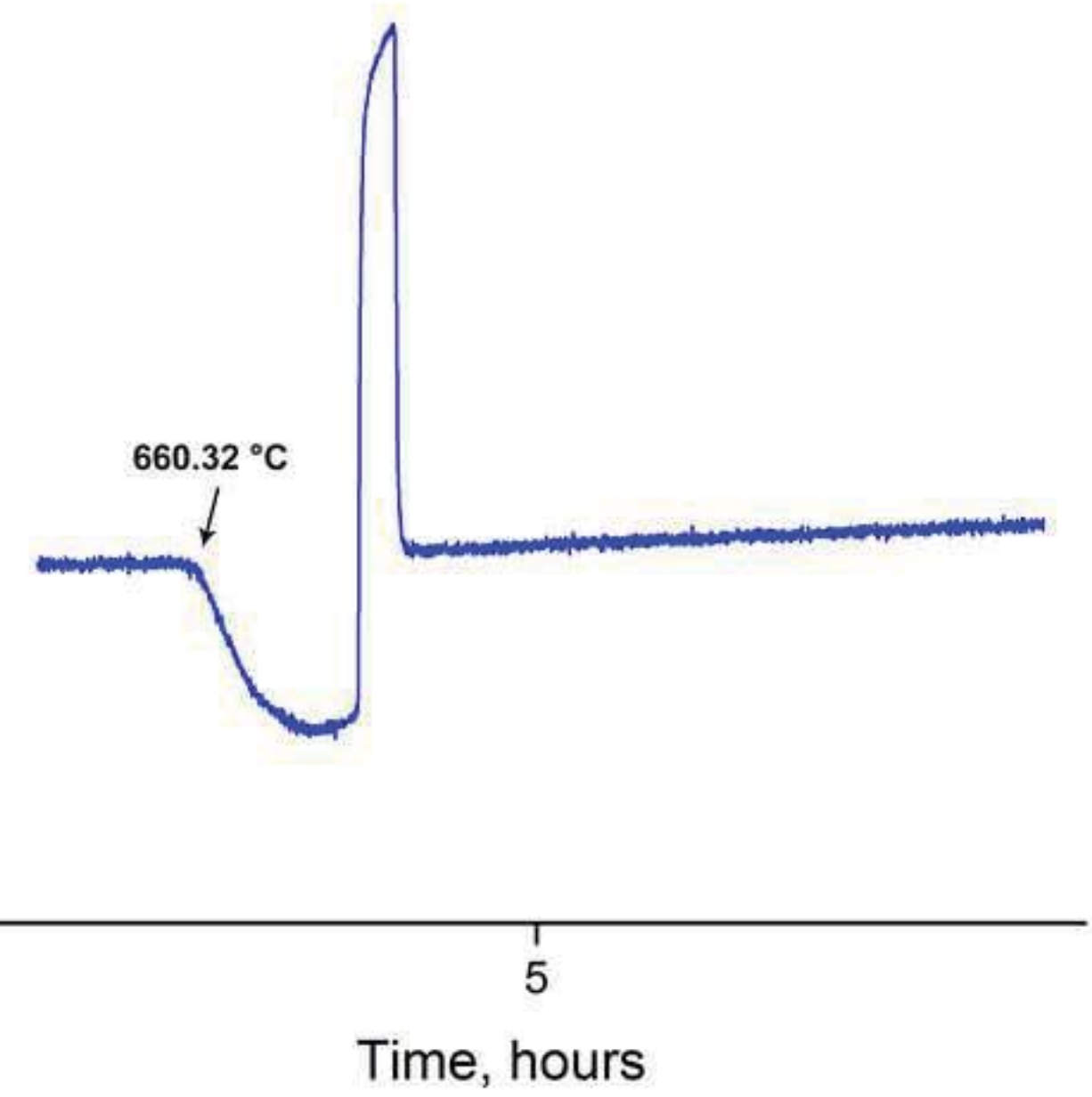

mage

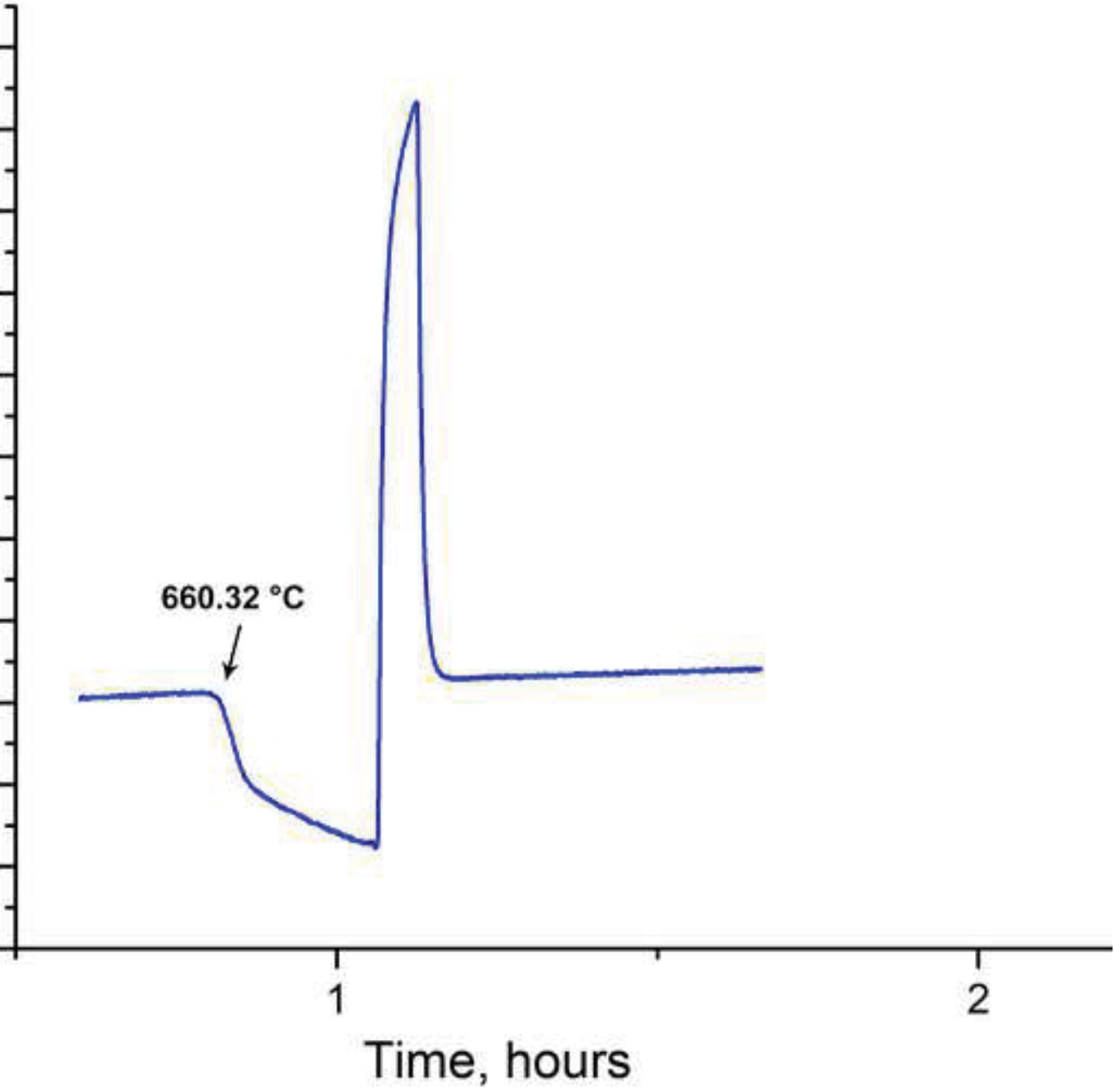

mage

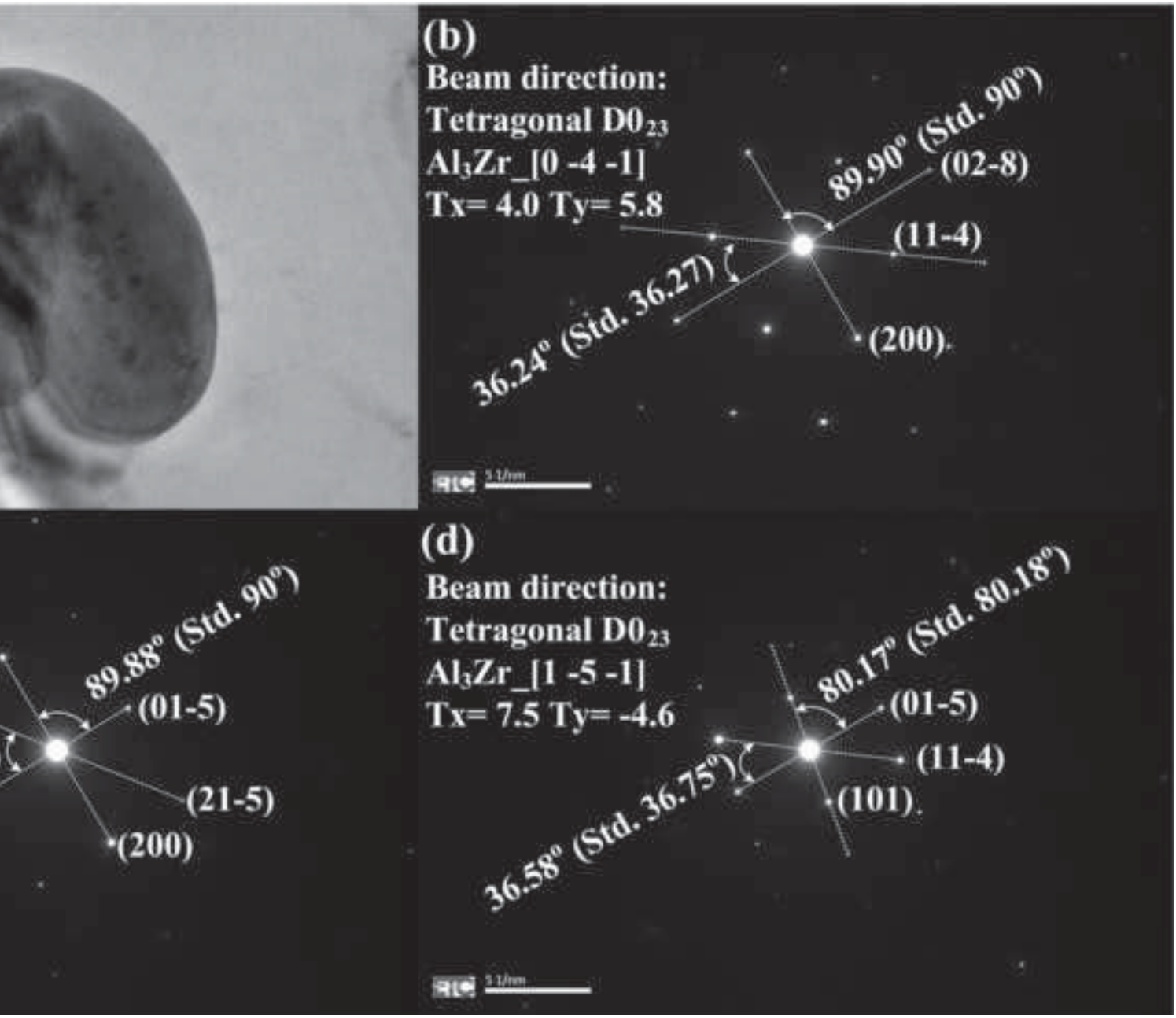
(b)
Beam direction:
Tetragonal D0$_{23}$
Al$_3$Zr_[0 -4 -1]
Tx= 4.0 Ty= 5.8
89.90° (Std. 90°)
(02-8)
(11-4)
36.24° (Std. 36.27)
(200)
5 1/nm
89.88° (Std. 90°)
(01-5)
(21-5)
(200)
(d)
Beam direction:
Tetragonal D0$_{23}$
Al$_3$Zr_[1 -5 -1]
Tx= 7.5 Ty= -4.6
80.17° (Std. 80.18°)
(01-5)
(11-4)
36.58° (Std. 36.75°)
(101)
5 1/nm